

# Using Nuclear Magnetic Resonance and the Dipolar Field to Study Structural Properties of Two-Phase Liquid Systems

by

Scott Michael Brown

B.S., Rensselaer Polytechnic Institute (1991)

M.B.A., State University of New York at Albany (1999)

Submitted to the Department of Nuclear Engineering  
in partial fulfillment of the requirements for the degrees of  
Nuclear Engineer

and

Master of Science

at the

MASSACHUSETTS INSTITUTE OF TECHNOLOGY

September 2001

© Scott M. Brown. All rights reserved.

The author hereby grants to MIT permission to reproduce  
and to distribute publicly paper and electronic  
copies of this thesis document in whole or in part.

Signature of Author .....

Department of Nuclear Engineering

Certified by .....

August 2, 2001

David G. Cory

Professor of Nuclear Engineering

Certified by .....

Thesis Supervisor

Neil E. Todreas

Professor of Nuclear Engineering

Thesis Supervisor

Accepted by .....

Jeffrey A. Coderre

Chairperson, Department Committee on Graduate Students

**DISTRIBUTION STATEMENT A**

Approved for Public Release

Distribution Unlimited

20011023 024

# Using Nuclear Magnetic Resonance and the Dipolar Field to Study Structural Properties of Two-Phase Liquid Systems

by

Scott Michael Brown

Submitted to the Department of Nuclear Engineering  
on August 2, 2001, in partial fulfillment of the  
requirements for the degrees of  
Nuclear Engineer  
and  
Master of Science

## Abstract

Nuclear Magnetic Resonance (NMR) is a convenient and noninvasive means for studying the internal structure of diamagnetic substances. The extraction of length scale information in liquid NMR spectroscopy is largely limited to sizes below the diffusion length ( $\sim 50$  microns). Breaking translational symmetry using the nuclear dipolar field imparts a scale dependence, and provides a means of measuring length scales above this limit.

The use of the dipolar field in liquid NMR to make structural measurements is a relatively novel concept in the field, and previous techniques have been largely limited to test cases. This thesis examines the extraction of length-scale information from a relatively complex two-phase liquid system, specifically a poly-disperse oil/water emulsion. Theory is developed and then compared to experimental results, with good agreement. Simple scaling laws are identified which provide a simple means of using the technique for length scale measurements. The thesis then focuses on developing the theory and feasibility of using the developed dipolar NMR technique to study flowing systems, in order to extract average length scale and interfacial properties, including interfacial velocity and interfacial area.

Thesis Supervisor: David G. Cory  
Title: Professor of Nuclear Engineering

Thesis Supervisor: Neil E. Todreas  
Title: Professor of Nuclear Engineering

# Acknowledgements

First, I would like to thank Professor David Cory for his exceptional guidance and support on this project. His insight has been invaluable, and I have learned a tremendous amount while working with him. I thank Professor Todreas for introducing me to the topic, and for helping to steer my efforts. I give a special thanks to Pabitra Sen for his contribution of time and effort to see this project through to completion. I also want to thank Chandrasekhar Ramanathan for his help on the mathematics involved with the velocity calculations, and all members of the “Cory Lab” for helping me learn the details needed to complete this thesis.

I thank the U.S. Navy for giving me the opportunity and financial support to make this contribution to the scientific community.

Finally, I would like to thank my family for their understanding and devotion. They provide the inspiration for all that I do.

# Contents

<b>1</b>	<b>Introduction</b>	<b>9</b>
1.1	Basics of NMR . . . . .	10
1.2	Thesis Goals . . . . .	11
<b>2</b>	<b>Background</b>	<b>13</b>
2.1	Basics of the Dipolar Field and Motional Narrowing in Liquids . . . . .	13
2.1.1	Basic Description of the Dipolar Field . . . . .	14
2.1.2	Motional Narrowing in Liquids . . . . .	16
2.2	Reintroducing the Dipolar Field in Liquid State NMR . . . . .	18
2.2.1	Multiple Echoes in $^3\text{He}$ and Liquids at High Magnetic Field . . .	18
2.2.2	The Dipolar Field in Solution NMR . . . . .	22
2.2.3	Structural Investigations Using the Dipolar Field . . . . .	25
2.3	Possible Applications for Two-Phase Flow Modeling . . . . .	28
2.3.1	Two-Fluid Model Description . . . . .	29
2.3.2	Field Equations and Closure Relations . . . . .	30
2.3.3	Interfacial Area . . . . .	34
2.3.4	Interfacial Velocity and Shear . . . . .	36
<b>3</b>	<b>Signal Physics</b>	<b>39</b>
3.1	Theory . . . . .	41
3.1.1	Basic Experiment and Overview . . . . .	42



3.1.2	Calculation of the Magnetic Field in an Oil Bubble . . . . .	43
3.1.3	Calculation of the Magnetization in the Oil Bubble . . . . .	49
3.2	Experiments and Discussion . . . . .	53
3.3	Conclusive Remarks Regarding Signal Physics . . . . .	58
<b>4</b>	<b>Signal Behavior and Interfacial Properties</b>	<b>59</b>
4.1	Scaling Behavior in the Long Wavelength Region . . . . .	61
4.2	Scaling Behavior in the Short Wavelength Region . . . . .	64
4.3	Discussion . . . . .	68
4.4	Interfacial Velocity . . . . .	70
4.5	Interfacial Area . . . . .	76
4.6	Laser Polarized Xenon . . . . .	81
<b>5</b>	<b>Conclusion and Future Research</b>	<b>84</b>
<b>A</b>	<b>Calculation of Equilibrium Magnetization</b>	<b>87</b>
	<b>Bibliography</b>	<b>89</b>

# List of Figures

2-1	Pulse sequence used by Bowtell to study indirect effects of the dipolar field.	22
2-2	"Crazed" sequence used by Warren et.al. . . . .	23
2-3	Pulse sequence used by Bowtell for coaxial cylindrical experiments. . . .	26
2-4	Flow regimes defined in the TRAC-M code. . . . .	34
3-1	Pulse sequence for emulsion experiment. . . . .	42
3-2	Coordinate system and problem setup for the mean field calculation. . . .	45
3-3	Parametric plot of the field intensity within an oil bubble ( $\Lambda_{q_m} = .5$ , $q_m \delta = \frac{2\pi}{3}$ ) . . . . .	48
3-4	X-component of the oil magnetization versus $z$ . . . . .	50
3-5	Comparison of experimental to model results ( $D_{mean} = 180\mu m$ ) . . . . .	52
3-6	Susceptibility fields around an oil bubble. . . . .	53
3-7	NMR spectrum of the emulsion sample. . . . .	54
3-8	Comparison of buildup curves showing sensitivity to mean diameter . . .	57
4-1	Variation of the signal ratio versus applied wavelength $\lambda$ . Insets show field intensity. . . . .	60
4-2	Coordinate system and problem setup for the slab problem. . . . .	65
4-3	Coordinate system and problem setup for polar region calculation. . . . .	67
4-4	Coordinate system and problem setup for interfacial velocity calculation.	71
4-5	Plots of the signal ratio versus $v_o$ and $t$ for $q_m = 3 \text{ mm}^{-1}$ . . . . .	73
4-6	Plots of the signal ratio versus $v_o$ and $q_m$ for $t = 5 \text{ msec}$ . . . . .	73

4-7	Plots of the signal ratio versus $t$ and $q_m$ for $v_o = .01$ m/s. . . . .	74
4-8	Example stroboscopic pulse sequence with $n = 2$ . . . . .	74
4-9	Plot of the signal ratio ( $n = 20$ ) and interval time for the stroboscopic velocity experiment. . . . .	75
4-10	Required water equilibrium magnetization to acheive a $SR = .01$ for static experiment. . . . .	79
4-11	Required equilibrium water magnetization to acheive a $SR = .01$ for $v_o =$ .05 m/s. . . . .	79
4-12	Required water equilibrium magnetization needed to achieve a Xe $SR =$ .01 ( $P = 4\%$ ) ans $SR = .005$ ( $P = 8\%$ ) for $v_o = .1$ m/s. . . . .	83

# List of Tables

3.1	Comparison of three NMR experiments used for size determination . . .	40
4.1	Comparison of Xe-129 and Water Proton Properties . . . . .	82

# Chapter 1

## Introduction

Nuclear Magnetic Resonance (NMR) is a convenient and noninvasive method of observing physical phenomena on both macroscopic and microscopic scales. It is a growing field that continues to expand its influence in the medical, industrial and scientific communities. The specific use of nuclear magnetic resonance for studying two-phase static systems is well developed for length scales on the order of several microns ( $\lesssim 50\mu\text{m}$ ). However, the present NMR techniques are not well-suited for measuring length scales above this limit. In addition, NMR has been investigated for measuring velocity distributions and void fractions in single and two-phase flowing systems<sup>1</sup>. These techniques use simple pulse gradient spin echo (PGSE) experiments, but are not suited for extracting length scales and studying interfacial properties, such as interfacial area and shear. This thesis will attack these difficult problems in order to provide a means to better characterize two-phase systems. Specifically, a relatively new concept in liquid NMR, the dipolar demagnetizing field (DDF), will be applied to the establishment of an electromagnetic connection, or correlation, between phases. The interaction provides a novel means of probing interfacial features of these systems.

---

<sup>1</sup>S. Javelot, "Creation of an NMR device to Characterize Multi-phase Flows", Doctorate Thesis, Pierre and Marie Curie University, 1994.

## 1.1 Basics of NMR

When an nucleus with spin-1/2 is placed in an external magnetic field ( $\vec{B}_o$ , or Zeeman field, aligned along the  $z$ -direction), the energy levels of the system separate into two distinct levels corresponding to the  $z$ -component of angular momentum (or spin states) of the system. The higher level energy state aligns in the opposite direction of the external field, and the lower energy state is aligned with the field. At equilibrium, the number of spins in the lower energy state is greater than the number in the higher energy state, giving the sample a net macroscopic magnetization,  $\vec{M}$ , along the direction of the main field. The net magnetization obeys the following equation of motion,

$$\frac{d\vec{M}}{dt} = \gamma \vec{M} \times \vec{B} \quad (1.1)$$

where  $\gamma$  is the gyromagnetic ratio. At equilibrium, the only field that is present is the static main field, and there is no torque placed on the magnetization. When the net magnetization vector is aligned along a different direction than the main magnetic field,  $\vec{B}_o$  (defined to be along the  $z$ -direction), the magnetization vector obeys Eqn. (1.1) and precesses around the main field at a given frequency known as the Larmor frequency,  $\omega_o$ . NMR net magnetization can be manipulated by applying external field pulses at the Larmor frequency transverse to the direction of the main field. A pulse rotates  $\vec{M}$ , and the amount of rotation is directly under experimental control. After the pulse duration,  $\vec{M}$  rotates at  $\omega_o$  around  $\vec{B}_o$ . However, the rotation does not continue forever. There are additional factors included in Eqn. (1.1) that cause the magnetization to relax. Spin-lattice relaxation, modeled using a  $T_1$  relaxation constant, drives the magnetization back to the equilibrium state. Spin-spin relaxation, modeled using a  $T_2$  relaxation constant, is caused by the dephasing of separate spins within the sample, and is responsible to the decay of the transverse magnetization. In addition, a modulated form of magnetization is attenuated by diffusion.

The basic NMR experiment is conducted in a frame of reference that is rotating close

to the Larmor frequency. As the spins relax back to the equilibrium state, they carry information in the form of the Larmor frequency, which is a function of the particular nucleus and the local field surrounding that nucleus. A simple Fourier transform of the signal in this rotating frame of reference reveals the frequency spectrum, and thus the type and number of nuclei in the sample, plus information regarding the sample character in the form of local fields.

This section has highlighted the basic NMR experiment. Obviously NMR gets very complex, and this thesis will go well beyond these basics to study the behavior of the local field produced at one type of nucleus resulting from the presence of another type of nucleus in a different phase. Specifically, how does a given macroscopic distribution of magnetization in one phase affect the evolution of the magnetization in another phase. The technique can be thought of as a scattering experiment, much like neutron scattering. The wave-vector of the source phase is effectively transferred to the second phase and then decoded. The resulting signal in the receiving phase inherently contains information on the system's average length scale, and provides an opportunity for further research into the global characteristics and behavior of two-phase systems.

## 1.2 Thesis Goals

The following list summarizes the goals for this thesis:

- 1) Develop the underlying physical model used to extract structural information using the nuclear dipolar field from a relatively complex heterogeneous system.
- 2) Verify the physics and model by comparison to a static NMR experiment (emulsion system).
- 3) Develop simple scaling laws that can be applied to easily extract length scale information.

- 4) Theoretically investigate use of the dipolar technique for studying interfacial velocity between two phases.
- 5) Investigate the feasibility of using the technique to make length scale measurements in two-phase flowing systems.

Chapter 2 provides background information regarding the dipolar mean field and its previous use for simple structural measurements and 2-D NMR. This chapter describes the history of the dipolar field technique, and also provides an introduction to an important possible application of the technique to two-phase flow modeling. Chapter 3 will tackle the first and second goals. The theory is developed using real space coordinates and basic Maxwell equations. The basic static experiment is demonstrated on an oil-water emulsion, an important representation of complex, heterogeneous soft matter. The full experiment is described and compared to theory with positive results. Chapter 4 develops the scaling behavior for the third goal and further compares theory to experiment. The scaling laws provide a simple method for using the technique to extract average length scale information. Chapter 4 also develops the theory and feasibility studies for the fourth and fifth goals. The basic theory is outlined with recommendations for further experiments and research. Finally, Chapter 5 summarizes the thesis results and provides additional recommendations for future research.

The focal point of the theoretical development is on the static experiment, where the two phases are fixed in position. After development of the static scaling behavior, the analysis uses simple scaling laws to further extrapolate the theory to include relative motion between the phases. The first velocity experiment is a simple sliding system in a slab geometry where one phase is sliding over the other. The effect of the relative velocity on the dipolar signal is examined, with the future goal of mapping out the interfacial velocity profile. The second dynamic experiment involves a more complex system, possibly bubbly two-phase flow where the goal is extraction of length scale information. The behavior is examined, and the feasibility of future work using liquid-liquid and gas-liquid systems is discussed.



# Chapter 2

## Background

This chapter describes the background associated with using the NMR dipolar field to study structural characteristics of two-phase systems. First, the basic NMR dipolar field is discussed, followed by a discussion of its associated development in the last decade. The subsequent sections of this chapter describe possible applications of NMR dipolar field technology for studying both static and flowing two-phase systems. Specifically for two-phase flow, a description is given regarding NMR applications for improving the current state of knowledge in computer code flow modeling.

### 2.1 Basics of the Dipolar Field and Motional Narrowing in Liquids

The dipolar field effect is very well known in the context of NMR, especially when applied to solids. Credit for the first formal quantitative evaluation of the dipolar demagnetizing field as currently applied to liquids is typically given to Deville et. al.<sup>1</sup> Most articles in the literature refer to their 1979 paper in the course of introducing the topic. With improvements in magnetic field and NMR technology, along with a better understanding

---

<sup>1</sup>Deville G., Bernier M., Delrieux J., "NMR Multiple Spin Echoes Observed in Solid  $^3\text{He}$ ", *Physical Review B*, Volume 19, Number 11, 1 June 1979, pp. 5666-5687.

of the physics behind dipolar effects in liquids, the examination and use of these effects for NMR spectroscopy and imaging techniques has risen dramatically in the last decade.

The dipolar field applies generally to all materials studied using NMR. After the general discussion of dipolar effects, the section explains why the effects are not typically observed in liquid state NMR.

### 2.1.1 Basic Description of the Dipolar Field

The spinning nucleus of an atom (assume a hydrogen-1 atom or simply a proton) with a given angular momentum gives rise to a magnetic dipole moment as discussed in the previous chapter. The classical field associated with this localized dipole has the following form<sup>2</sup>

$$\vec{B}(\vec{R}) = \frac{\mu_o}{4\pi} \left[ \frac{3\hat{n}(\hat{n} \cdot \vec{m}) - \vec{m}}{|\vec{R}|^3} \right] \quad (2.1)$$

where  $\vec{B}$  is the magnetic flux density,  $\vec{R}$  is the vector from the source point of the dipole to the observation point of the field,  $\vec{m}$  is the magnetic moment of the dipole,  $\hat{n}$  is the unit vector in the direction  $\vec{R}$ , and  $|\vec{R}|$  is the magnitude of  $\vec{R}$ . The potential energy,  $E$ , of a dipole in an external magnetic field is

$$E = -\vec{m} \cdot \vec{B} \quad (2.2)$$

Slichter<sup>3</sup> describes the derivation of the quantum mechanical form of the dipolar energy Hamiltonian by starting with the classical form of the interaction energy between two

---

<sup>2</sup>Jackson, J. D., **Classical Electrodynamics**, Third Edition, John Wiley and Sons, Inc., 1999, p. 186.

<sup>3</sup>Slichter, C. P., **Principles of Magnetic Resonance**, Third Edition, Springer, 1990, p. 66.

magnetic dipole moments, as determined from the above two equations

$$E = \frac{\vec{m}_1 \cdot \vec{m}_2}{r^3} - \frac{3(\vec{m}_1 \cdot \vec{r})(\vec{m}_2 \cdot \vec{r})}{r^5} \quad (2.3)$$

where  $\vec{r}$  is the radius vector from  $\vec{m}_1$  to  $\vec{m}_2$ . For the quantum mechanical description, we now treat  $\vec{m}_1$  and  $\vec{m}_2$  as operators for the atomic dipole moments

$$\begin{aligned} \vec{m}_1 &= \gamma_1 \hbar \vec{I}_1 \\ \vec{m}_2 &= \gamma_2 \hbar \vec{I}_2 \end{aligned} \quad (2.4)$$

$\vec{I}_1$  and  $\vec{I}_2$  are the angular momentum operators for the two spins. Then for  $N$  spins the general dipolar Hamiltonian equation is

$$\mathcal{H}_d = \frac{1}{2} \sum_{j=1}^N \sum_{k=1}^N \left[ \frac{\vec{m}_j \cdot \vec{m}_k}{r_{jk}^3} - \frac{3(\vec{m}_j \cdot \vec{r}_{jk})(\vec{m}_k \cdot \vec{r}_{jk})}{r_{jk}^5} \right] \quad (2.5)$$

where  $j \neq k$ . This equation can be simplified by writing  $\vec{m}_1$  and  $\vec{m}_2$  in component form, considering only two identical spins ( $\gamma_1 = \gamma_2 = \gamma$ ), expressing the  $x$  and  $y$  components of the angular momentum operators in terms of the raising and lowering operators, converting to spherical coordinates,  $r, \theta, \phi$ , and neglecting weak absorption terms in the expression. The final simplified form<sup>4</sup> is

$$\mathcal{H}_d = \frac{1}{4} \gamma^2 \hbar^2 \sum_{j,k} \frac{(1 - 3 \cos^2 \theta_{j,k})}{r_{j,k}^3} (3I_{jz}I_{kz} - \vec{I}_j \cdot \vec{I}_k) \quad (2.6)$$

$\theta$  is the angle between the  $z$ -axis and the vector  $\vec{r}_{jk}$ . This equation is often called the secular part of the dipolar Hamiltonian. It neglects all components of the dipolar field that rotate about the  $z$ -axis. These components are non-secular and very small (Intensities of their absorption modes are proportional to  $\left(\frac{B_d}{B_o}\right)^2$ ) and they can be safely neglected.

---

<sup>4</sup>Slichter, Ibid. p. 70.

In solids, each atom is surrounded by a fixed number of other atoms. Therefore, each nucleus effectively "sees" a large number of fixed dipoles. These dipoles have a strong effect on the dynamics associated with an NMR experiment, in that they effectively perturb the magnetic field of a given nucleus. The closer nuclei will give a more pronounced perturbation of the main magnetic field owing to the  $\frac{1}{r^3}$  behavior of the dipolar field. All nuclei therefore have an effect on the local field experienced by a given nucleus. Since the dipolar fields from the surrounding nuclei can either aid or oppose the main static field, there will be a spread in the Larmor frequency. The dipolar field is thus responsible for large line widths of solid sample spectra. This effect is included in a larger subset of line shape effects termed homogeneous broadening<sup>5</sup>. Homogeneous broadening occurs when each spin makes the same contribution to the line width, or, as in the case of solid single crystals, there are separate contributions caused by the dipolar field, but individual contributions cannot be identified. In contrast, an inhomogeneously broadened line is one in which the individual contributions to the line shape can be identified. For example, the line shape associated with an inhomogeneous main magnetic field,  $B_0$ , is broadened because each spin "sees" a different field and will precess at a different Larmor frequency. The inhomogeneous broadening can be removed by perfecting the shim, or homogeneity of the main magnetic field. Homogeneous broadening, on the other hand, will not be affected by the quality of the shim.

### 2.1.2 Motional Narrowing in Liquids

Liquid molecules are not located in any form of periodic lattice, and liquid molecules are continually moving at much faster rates than those of a solid. Slichter<sup>6</sup> gives a simple description of the effects of molecular motion on spin-spin relaxation, in which the spins are coupled to an external fluctuating field. Slichter's example gives all the qualitative

---

<sup>5</sup>Fukushima E., Roeder S., **Experimental Pulse NMR, A Nuts and Bolts Approach**, Addison-Wesley Publishing Company, 1981, pp. 218-219.

<sup>6</sup>Slichter, p.p. 212-213.

information necessary to describe the effects considering dipole-dipole coupling.

The following equation results from Redfield theory when considering an ensemble of spins coupled to an external fluctuating magnetic field.

$$\frac{1}{T_2} = \gamma_n \overline{H_z^2} \tau + \frac{1}{2T_1} \quad (2.7)$$

This is an equation relating  $T_2$ , the spin-spin relaxation constant, to  $T_1$ , the spin-lattice relation constant, the mean square local  $z$ -component of field,  $\overline{H_z^2}$ , and  $\tau$ , the motional correlation time of the fluctuating local magnetic field. A shorter  $\tau$  represents faster motion and a longer  $\tau$  represents slower motion. The first term in this equation is adequately derived by Slichter assuming that the local field,  $H_z$ , has a value  $|H_z|$ , for a period of time,  $\tau$ , and then changes randomly to  $\pm |H_z|$ . This field change occurs because, in liquids, a nucleus moves relative to its neighbors by diffusion. In each interval of time,  $\tau$ , a spin precesses a small phase angle, and the mean squared phase angle after time,  $t$ , or  $n = \frac{t}{\tau}$  intervals is<sup>7</sup>

$$\overline{\Delta\phi^2} = n\gamma^2 H_z^2 \tau^2 \quad (2.8)$$

Defining  $T_2$  as the time for the spins to get 1 radian out of phase results in the first term on the left side of Eqn. (2.7). Thus, as  $\tau$  decreases (the motion becomes more rapid)  $T_2$  increases resulting in a more narrow frequency spectrum line. This line narrowing is termed "motional narrowing". The motion narrows the line because the total dephasing takes place by a random walk of steps. When there is no motion, each spin experiences a constant field and precesses either slower or faster than the average. The total dephasing of a group of spins occurs because of the accumulation of positive or negative phase. The motional narrowing effect is the reason why dipolar effects are often neglected in the liquid state. However, as discussed in the following section, dipolar effects can be reintroduced by considering a long range mean dipolar field.

---

<sup>7</sup>Ibid., p. 212.

## 2.2 Reintroducing the Dipolar Field in Liquid State NMR

This section describes, in basic terms, how experimentalists have been able to reintroduce the effects of the dipolar field in liquid state NMR. Theoretically, the dipolar field effects in liquids can be explained using both a classical and quantum mechanical description. Both descriptions can be applied to describe experimental data, and each description has its own particular advantages depending on the type of experiment performed. The classical description is typically reserved for experiments involving multiple echoes and structural determinations. The quantum mechanical description has traditionally been used in solution 2D-NMR to describe the presence of intermolecular cross peaks and other phenomena for multi-component systems.

### 2.2.1 Multiple Echoes in $^3\text{He}$ and Liquids at High Magnetic Field

As stated before, credit for the first quantitative analysis of the mean dipolar field (also called the Dipolar Demagnetizing Field) is typically reserved for Deville et. al.<sup>8</sup>. Their studies focused on solid  $^3\text{He}$  NMR. Solid  $^3\text{He}$  atoms experience a large zero-point motion that contributes to motional narrowing and a long  $T_2$ . They discovered the unusual phenomenon of multiple echoes after two radio frequency (r.f.) pulses.. Typically, two r.f. pulses result in a single echo as given by Hahn<sup>9</sup>. Deville explained multiple echoes by considering a long range demagnetizing field  $B_d$  with a magnitude that was on the order of the nuclear equilibrium magnetization  $M_0$ . Since this field is typically very small, it does not significantly contribute to normal the dynamics of an NMR experiment. However, when transverse magnetization evolves in the presence of  $B_d$  over a time period

---

<sup>8</sup>G. Deville, M Bernier, and J.M. Delrieux, "NMR Multiple Echos Observed in solid  $^3\text{He}$ ", *Physical Review B*, **19** (11), June 1979, pp. 5666-5699.

<sup>9</sup>E.L. Hahn, "Spin Echoes", *Physical Review*, **80** (4), November 1950, pp. 580-594.

on the order of  $T_2$ , with  $\gamma B_d T_2 \geq 1$  the nonlinear effects of the field interaction play a significant role. One might think that motional narrowing would destroy the effects of the dipolar field. But the interaction that contributes to motional narrowing (the exchange interaction) is short ranged. Therefore, as the distance,  $r$ , between two spins increases, the fluctuations caused by the exchange interaction decrease, so that, at a critical distance, any long range dipolar interaction can dominate.

The experiments consisted of two pulses which placed a magnetization grating along the  $z$ -axis, and transverse magnetization then evolved in the presence of the longitudinal magnetization. The entire experiment was carried out under the presence of the applied gradient. They noted the usual spin echo, but also a number of other echoes, spaced at the same time intervals as the first echo (i.e., multiples of  $\tau$ , where  $\tau$  is the time between pulses).

Deville's analysis begins with the derivation of a simple form for  $B_d$ . By assuming a relatively large gradient is applied to the sample, the effects of the sample shape can be neglected, and the field becomes local and one dimensional. They derived

$$\vec{B}_d(s) = \frac{\mu_o}{2} [3(\hat{s} \cdot \hat{z})^2 - 1] \left[ M_z(s) \hat{z} - \frac{1}{3} \vec{M}(s) \right] \quad (2.9)$$

where  $\hat{s}$  is the direction of the applied gradient, and  $\hat{z}$  is the direction of the main magnetic field. This field affects the precession frequency, and must be included in the Bloch equations to determine its effect on the NMR signal. Neglecting relaxation, the Bloch equation becomes

$$\frac{d\vec{M}(s)}{dt} = \gamma \{ \vec{M}(s) \times [B_o + Gs + \mu_o \beta M_z(s)] \hat{z} \} \quad (2.10)$$

where  $\beta = \frac{3(\hat{s} \cdot \hat{z})^2 - 1}{2}$  and  $G$  is the applied gradient strength. This equation results because the components of  $B_d(s)$  parallel to  $\vec{M}(s)$  do not affect the precession of  $\vec{M}(s)$ .

The following example illustrates the calculation of the effects assuming no relaxation and a  $z$ -directed gradient, so that  $\beta = 1$ . The addition of the dipolar field to the Bloch

equations creates a nonlinear equation of motion. The complex magnetization represents the transverse magnetization, and can be given by

$$M^+ = M_x + iM_y \quad (2.11)$$

Solutions of Eqn. (2.10) give the following form for  $M^+$

$$M^+(s, t) = M_o e^{-i\gamma G s \tau} e^{i\gamma \mu_o M_z(s)t} \quad (2.12)$$

or

$$M^+(s, t) = M_o e^{-i\gamma G s t} e^{i\gamma \mu_o M_o \sin(\gamma G s \tau) t} \quad (2.13)$$

for a sine modulated longitudinal magnetization. The second exponential term in this equation can be expanded into

$$e^{i\gamma \mu_o M_o \sin(\gamma G s \tau) t} = \sum_{n=-\infty}^{\infty} J_n(\gamma \mu_o M_o t) e^{in\gamma G s \tau} \quad (2.14)$$

Thus, when  $t = n\tau$ , the two exponential terms will cancel and the magnitude of the echo will be  $J_n(\gamma \mu_o M_o t)$ . This process explains why numerous echoes are observed after the application of the second pulse. The continuously applied external gradient refocuses the spatial components at integer multiples of the spatial encoding wave number when the evolution time,  $t$ , is an integer multiple of  $\tau$ . Deville's paper goes into the determination of the signal magnitude considering the effects of relaxation and diffusion. However, the general conclusion of refocusing spatial Fourier components remains unchanged. Only the amplitude of the echoes is changed.

Bowtell<sup>10</sup> and Körber<sup>11</sup> did additional studies of dipolar field effects in the early

---

<sup>10</sup>R. Bowtell, R.M. Bowley, and P. Glover, "Multiple Spin Echoes in Liquids in a High Magnetic Field", *Journal of Magnetic Resonance*, **88**, 1990, pp. 643-651.

<sup>11</sup>Harold Körber, Elmar Dormann, and Goerg Eska, "Multiple Spin Echoes for Protons in Water",



1990's. They were studying liquid systems, and noted the same effects in these systems that Deville noted. The higher magnet strengths available at this time made the effects apparent. Again the results were attributed to the long range dipolar field. In the same volume of the *Journal of Magnetic Resonance* as Körber's paper above, Bowtell<sup>12</sup> described an investigation of multiple spin echoes in multicomponent liquids. He noted the effects of the dipolar field from one substance in a two-component solution on the other substance. They noted that the total amplitude of the second echo was modulated at the beat frequency of the chemical shifts,  $\gamma B_o(\delta_1 - \delta_2)$ , where  $\delta_1 - \delta_2$  is the chemical shift between the two species. The additional echoes were also modulated.

The next year, Bowtell<sup>13</sup> published his work on using the dipolar field to indirectly detect the magnetization of a spin species. The method employed separate channels so that each component in the system could be separately excited, and the experiments were conducted in a continuously applied gradient field. The pulse sequence is shown in Figure (2-1). Obviously, no echo would be observed on the I-spin channel if the dipolar field was not present. The echo occurs because the transverse magnetization of the I-spin is perturbed by the field of the S-spin. The Fourier components of the resulting I-spin magnetization are unwound by the applied gradient and an echo results. If diffusion and relaxation are neglected, the transverse I-magnetization after the  $90^\circ$  pulse is

$$M_I^+(t) = M_{Io} \sum_{n=-\infty}^{\infty} J_{|n|} \left( \frac{2}{3} \mu_o \gamma_I M_{So} t \right) e^{i\gamma_I G z \left[ \frac{(n\tau' \gamma_S)}{\gamma_I} - t \right]} \quad (2.15)$$

where echoes occur at times  $t = n\tau = n\tau' \frac{\gamma_S}{\gamma_I}$ . The I-magnetization is unwound by the gradient at a rate  $\left( \frac{\gamma_I}{\gamma_S} \right)$  times the rate at which the S-magnetization is wound up. This study showed that the presence of the dipolar field could allow indirect detection provided that the species were intermingled on a microscopic scale. At this time, the usefulness of

---

*Journal of Magnetic Resonance*, **93**, 1991, pp. 589-595.

<sup>12</sup>A.S. Bedford, R. Bowtell, and R.M. Bowley, "Multiple Spin Echoes in Multicomponent Liquids", *Journal of Magnetic Resonance*, **93**, 1991, pp. 516-532.

<sup>13</sup>R. Bowtell, "Indirect Detection via the Dipolar Demagnetizing Field", *Journal of Magnetic Resonance*, **100**, 1992, pp. 1-17.

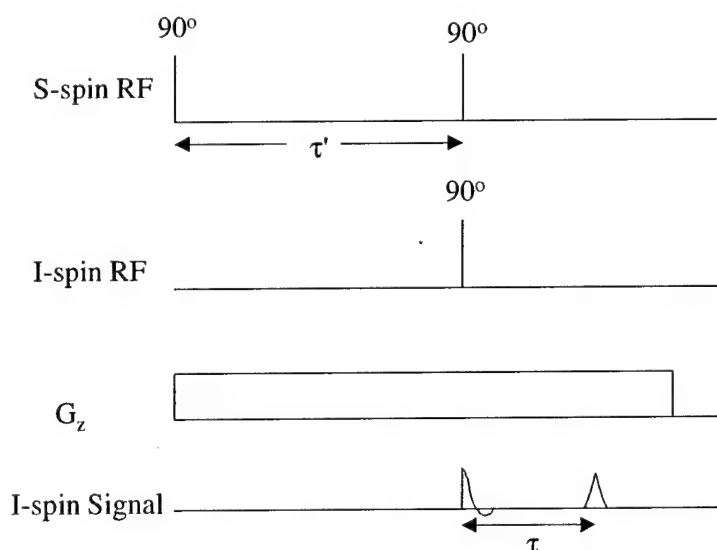


Figure 2-1: Pulse sequence used by Bowtell to study indirect effects of the dipolar field.

the dipolar technique lay in the fact that, under certain circumstances, it could produce a signal-to-noise ratio (SNR) that was greater than direct detection. This increase in SNR could occur by detecting a low  $\gamma$  spin via a large  $\gamma$  spin, say protons. However, the gain in SNR was still less than could be obtained using other established methods.

## 2.2.2 The Dipolar Field in Solution NMR

Study of the dipolar field in the context of solution 2D-NMR stemmed from Warren et al.'s work<sup>14</sup> regarding the presence of intermolecular cross peaks. They showed that relatively simple pulse sequences generated cross peaks between bulk water and a glycoprotein fragment. Cross peaks are associated with intermolecular multiple quantum coherences.

Warren's work centered on the pulse sequence described by Figure (2-2). He named this sequence the "Crazed" sequence. The sequence looks much like a COSY sequence,

<sup>14</sup>Warren S. Warren, Wolfgang Richter, Amy Hamilton Andeotti, and Bennet T. Farmer II, "Generation of Impossible Cross-Peaks Between Bulk Water and Biomecules in Solution NMR", *Science*, Vol. 262, December 1993, pp. 2005-2009.

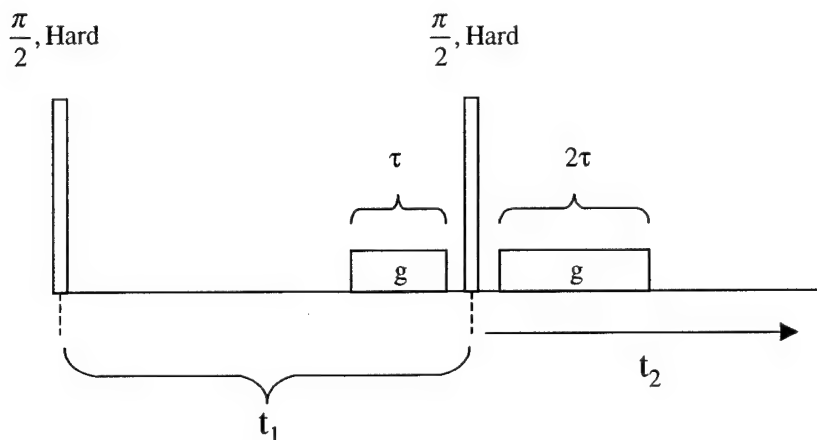


Figure 2-2: "Crazed" sequence used by Warren et.al.

and the presence of an intermolecular cross peak could only result from double quantum coherences across molecules. The only realistic coupling to create the coherence is the dipolar coupling, but it is generally assumed to be negligible owing to diffusion and motional narrowing, as discussed earlier. Warren attributed the presence of cross peaks to the long range dipolar coupling between spins separated by distances greater than diffusion lengths on an NMR time scale ( $\sim 10 \mu\text{m}$ ). The presence of a non-isotropic distribution of dipoles broke the symmetry and reintroduced the dipolar coupling. He used a density matrix approach to study the NMR signal characteristics, and he discarded the usual high temperature approximation,  $\rho_{eq} \approx 1 - \left(\frac{\gamma B_o}{kT}\right) I_z$ , where  $\rho_{eq}$  is the equilibrium density matrix,  $\gamma$  is the gyromagnetic ratio,  $B_o$  is the applied static magnetic field,  $k$  is the Boltzman constant,  $T$  is the temperature, and  $I_z$  is the magnetization in the  $z$ -direction. The first neglected term  $\frac{1}{2} \left[ \left(\frac{\gamma B_o}{kT}\right) I_z \right]^2$  is very small as  $\left(\frac{\gamma B_o}{kT}\right) \approx 10^{-4}$ . However, Warren shows that the presence of extra terms in the density matrix, the extra dipolar terms, and such an enormous number of spins in a given sample, transfers intermolecular multiple quantum coherences into observable magnetization. The normalized signal magnitude,

using Warren's approach, is

$$\text{Crazed Signal} = \frac{3}{32\pi} M_o t_2 \gamma \mu_o \int_V \frac{(3 \cos^2 \theta - 1)}{r^3} \cos(\gamma g s \tau) r^2 \sin \theta dr d\theta d\phi \quad (2.16)$$

If not for the presence of the  $\cos(\gamma g s \tau)$  term in Eqn. (2.16), the angular integration results in zero signal. The cosine modulation acts to break the symmetry, and reintroduce the dipolar effects. This equation must be integrated over the sample volume minus a sphere of radius  $r_{cutoff} = 10 \mu\text{m}$ . For simplicity, Warren integrated over a spherical sample. Warren first plotted the function  $F(\gamma g \tau r)$  defined by

$$(\gamma g \tau) F(\gamma g \tau r) \frac{[3(\hat{s} \cdot \hat{z})^2 - 1]}{2} = \int_{\theta=0}^{\pi} \int_{\phi=0}^{2\pi} \frac{(3 \cos^2 \theta - 1)}{r^3} \cos(\gamma g s \tau) r^2 \sin \theta d\theta d\phi \quad (2.17)$$

versus  $\gamma g \tau r$  radians. Physically,  $F(\gamma g \tau r)$  is the effectiveness of the long-range dipolar Hamiltonian in transferring coherence from slowly modulated two-spin operators into observable magnetization. This function showed that the majority of the crazed signal resulted when  $\gamma g \tau r$  was between 2 and 4, and that the calculation converges as  $r \rightarrow \infty$ . Thus, the majority of the signal results from spins within about half of the wavelength of the applied grating. In addition, the logarithmic divergence associated with the radial integration was broken. Warren then continued with the radial integration and showed that

$$\text{Crazed Signal} = \frac{1}{4} \frac{t_2}{\tau_d} \frac{[3(\hat{s} \cdot \hat{z})^2 - 1]}{2} \quad (2.18)$$

where  $\tau_d = \frac{1}{M_o \gamma \mu_o}$  is the "dipolar demagnetizing time". The combined contribution of the very small dipolar couplings and the small additional terms in the equilibrium density matrix resulted in a signal that was comparable in magnitude to that produced by a single  $\frac{\pi}{2}$ -pulse. Finally, Warren noted that the dependence of the dipolar range on the gradient strength could possibly lead to applications for structural measurements.

Warren has continued to enhance and build upon the quantum mechanical formalism to study the effects of the dipolar demagnetizing field in solution NMR<sup>15,16,17</sup>. Several comparisons have been made between the "classical" and "Warren" approaches to solving the dipolar problem. Jeener<sup>18</sup> lays to rest all concerns regarding the equivalence of the two approaches. Basically, the classical approach uses the mean field resulting from a magnetization distribution and neglects individual couplings between molecule, while the quantum mechanical approach retains the couplings, but assumes that diffusion destroys couplings close to any given molecule.

### 2.2.3 Structural Investigations Using the Dipolar Field

In 1996, Bowtell<sup>19</sup> published a paper that discussed the use of the dipolar field to probe structural properties in solution NMR using multiple spin echoes (MSE). The technique was similar to the indirect detection technique, but the study dealt only with protons in two different components. Thus, the chemical shift between compounds distinguished the protons in the NMR frequency spectrum. Bowtell experimentally studied a coaxial cylindrical system in which the outer glass tube contained water (component 1) and the inner glass tube contained acetone (component 2). The pulse sequence is shown in Figure (2-3). The first two selective pulses rotate the magnetization of component 1 onto the longitudinal axis, and the first gradient modulates this longitudinal magnetization. The crusher gradient removes all remaining transverse magnetization. The second component

---

<sup>15</sup>S. Lee, W. Richter, S. Vathyam, and W.S. Warren, "Quantum Treatment of the Effects of Dipole-Dipole Interactions, in Liquid Nuclear Magnetic Resonance", *J. Chem. Phys.*, **105** (3), July 1996, pp. 874-900.

<sup>16</sup>Warren S. Warren and Sangdoo Ahn, "The Boundary Between Liquidlike and Solidlike Behavior in Magnetic Resonance", *J. Chem. Phys.*, **108** (4), January 1998, pp. 1313-1325.

<sup>17</sup>Sangdoo Ahn, Natalia Lisitza, and Warren S. Warren, "Intermolecular Zero-Quantum Coherences of Multi-Component Spin Systems in Solution NMR", *Journal of Magnetic Resonance*, **133**, 1998, pp. 266-272.

<sup>18</sup>J. Jeener, "Equivalence between the "Classical" and the "Warren" Approaches for the Effects of Long-Range Dipolar Couplings in Liquid Nuclear Magnetic Resonance", *J. Chem. Phys.*, **112** (11), March 2000, pp. 5091-5094.

<sup>19</sup>R. Bowtell and P. Robyr, "Structural Investigations with the Dipolar Demagnetizing Field in Solution NMR", *Physical Review Letters*, **76** (26), June 1996, pp.4971-4974.

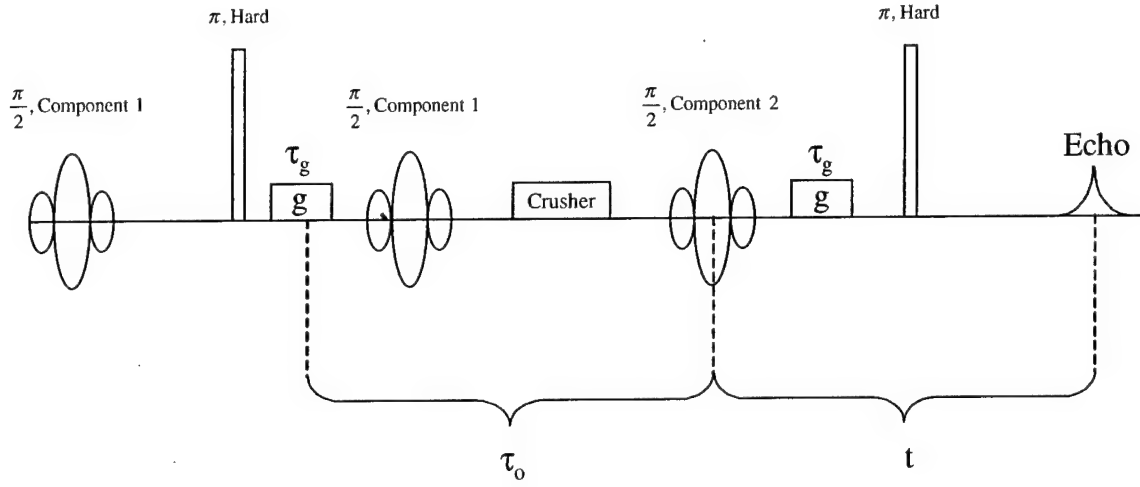


Figure 2-3: Pulse sequence used by Bowtell for coaxial cylindrical experiments.

is then excited by the final selective pulse, and the final gradient modulates the transverse magnetization at the same wavelength as the surrounding water. The  $\pi$ -pulses serve to refocus transverse magnetization and do not affect the evolution of the MSE. Bowtell explained the experimental results by considering the Fourier transformed form of the dipolar field,

$$\vec{B}^{dip}(\vec{k}) = \frac{-\mu_o}{3} \frac{3(\hat{k} \cdot \hat{z})^2 - 1}{2} [\vec{M}(\vec{k}) - 3M_z(\vec{k})\hat{z}] \quad (2.19)$$

where

$$\vec{B}^{dip}(\vec{k}) = \int_{-\infty}^{\infty} e^{-i\vec{k} \cdot \vec{r}} B^{dip}(\vec{r}) d^3r \quad (2.20)$$

and

$$\vec{M}(\vec{k}) = \int_{-\infty}^{\infty} e^{-i\vec{k} \cdot \vec{r}} \vec{M}(\vec{r}) d^3r \quad (2.21)$$

The study also assumed that the dipolar field generates a small perturbation of the local magnetization so that the time evolution equation becomes

$$\delta \vec{M}(\vec{r}, t) = \vec{M}(\vec{r}, t) - \vec{M}(\vec{r}, 0) \approx \gamma \vec{M}(\vec{r}, 0) \times \vec{B}^{dip}(\vec{r}) t \quad (2.22)$$

This equation assumes that the magnetization builds up linearly over the time range of the experiment ( $\gamma B^{dip} t \ll 1$ ).

The analysis consisted of Fourier transforming the equilibrium magnetization of each species over their respective sample volumes, and then, after considering the effect of the pulse sequence, integrating Eqn. (2.22) over all  $k$ -space to arrive at the signal magnitude for a given evolution time and modulation wave number. The study compared the signals generated with different cylinder thicknesses and spacings. The signal clearly changed depending on the particular arrangement, and the study showed that structural aspects could be probed using the dipolar field.

Bowtell has continued to build upon his classical analysis to study dipolar field effects. In another paper<sup>20</sup>, his group used the above technique to study packed glass beads of a certain diameter in a surrounding water matrix. The techniques were very successful at fitting the derived signal curves to the experimental data in order to extract the diameter. In another study<sup>21</sup>, the group studied randomly packed microspheres of identical size, and then interpreted the results in the form of a spatial autocorrelation, or Patterson, function

$$P_M(\vec{r}) = \frac{1}{M_{total}} \int_{-\infty}^{\infty} M_o(\vec{r}') M_o(\vec{r}' + \vec{r}) d^3 r' \quad (2.23)$$

---

<sup>20</sup>P. Robyr and R. Bowtell, "Nuclear Magnetic Resonance Microscopy in Liquids Using the Dipolar Field", *J. Chem. Phys.*, **106** (2), January 1997, pp. 467-476.

<sup>21</sup>P. Robyr and R. Bowtell, "Measuring Patterson Functions of Inhomogeneous Liquids Using the Nuclear Dipolar Field", *J. Chem. Phys.*, **107** (3), July 1997, pp. 702-706.

where

$$M_{total} = \int_{-\infty}^{\infty} M_o(\vec{r}) d^3r \quad (2.24)$$

Using their techniques and observing the Patterson functions, they were able to extract the diameter of the beads with reasonably good accuracy. The proposed main benefit of the study was that it potentially widened the applicability of using the dipolar field because the results did not requiring fitting data using a complex model. The Patterson functions tended to give a broad minimum at modulation gratings corresponding to the size of the spheres. However, in each of the above papers described in this paragraph, the dipolar signal resulted from interactions between a single species, water. The experiments did not transfer magnetization to another species, as had been done with the cylindrical studies. In addition, the physical nature of the field behavior was partially masked by the mathematical techniques used in the study.

## 2.3 Possible Applications for Two-Phase Flow Modeling

One aspect of this thesis will be to investigate the feasibility of using the NMR dipolar field to make interfacial structural and velocity measurements for two-phase flowing systems. The basic premise is to limit the NMR signal to a region that is close to the interface. Then extract the necessary information (structure or relative velocity). The next few sections will introduce the necessary variables required to solve the two-phase flow modeling problem, and discuss the current state of the art regarding experimental determination of these parameters.

Thermal hydraulic computer codes are invaluable for the design and validation of complex reactor systems. They are developed to study steady state as well as transient accident scenarios. Most codes rely on a two-fluid framework, where each phase is mod-



eled with its own set of field equations. The codes solve for all necessary variables, subject to boundary and initial conditions. This section will focus on interfacial parameters in the codes and models. Specifically, several examples of the Nuclear Regulatory Commission's (NRC) TRAC-M code are used in order to explain the importance of several key closure relations, specifically the interfacial area and interfacial velocity. This code is representative of previously developed two-fluid codes. It is the most recently developed, and was developed to consolidate several other codes.

The field equations require closure laws, so that each phase can be coupled to allow for simultaneous solution of the necessary variables. Most two-fluid model codes solve similar field equations. However, differences exist regarding the methodologies for incorporating the closure relations. Closure relations must describe the phenomena of mass transfer, momentum transfer, and energy transfer between the phases. In addition, while the codes perform satisfactorily compared to experimental validation, there is a strong motivation for improving the accuracy of the codes to further improve safety and reduce design costs incurred by excessive design margins.

The Transient Reactor Analysis Code (TRAC) was developed by the NRC to provide advance simulations of transients for pressurized water reactors (PWR) and boiling water reactors (BWR)<sup>22</sup>. TRAC-M/F90 (M stands for Modernized, F90 stands for FORTRAN 90) is the newest version of the code developed using the standard FORTRAN 90 programming language. The present discussion will focus on the parameters used in the TRAC-M code, but the basic methodology and processes regarding solving the field equations are similar between different codes.

### **2.3.1 Two-Fluid Model Description**

As discussed above, a two-fluid model describes the flow based on modeling each distinct phase. For example, the TRAC-M code uses a four component, two-fluid model. The

---

<sup>22</sup>TRAC-M/FORTRAN 90 (VERSION 3.0) **Theory Manual**, J. W. Spore et al., U.S. NRC, July 2000.

four components are liquid water, liquid solute, water vapor, and non-condensable gas. The two fluids are liquid and gas. Since two phases are considered, the model requires six field equations for each phase. Two additional equations are necessary to model the liquid solute and non-condensable gas considerations in the model. The model solves the partial differential equations using a finite-difference technique to obtain solutions for the following eight variables

- Liquid and gas field velocities,  $V_l$  and  $V_g$
- Liquid and gas field temperatures,  $T_l$  and  $T_g$
- Void fraction,  $\alpha$
- Pressure,  $P$
- Partial pressure of non-condensables,  $P_a$
- Solute concentration,  $m$

In order to solve the eight equations, the model makes some basic assumptions. The most important assumptions are the quasi-steady state assumption, and the time and volume averaged form of the field equations.

### 2.3.2 Field Equations and Closure Relations

To solve the field equations, a number of closure relations are specified. For computer codes, the field equations are often one-dimensional and nodalized, assuming constant fluid properties in each node. Thus, typical codes remove all properties, such as density and void fraction, from inside differentials, and then evaluate the equations for a given node. The closure relations then couple the equations, which are solved simultaneously for the variables given in the previous section. Levy<sup>23</sup> gives the general two-fluid field

---

<sup>23</sup>Levy, S., **Two-Phase Flow in Complex Systems**, John Wiley and Sons, Inc., 1999, pp.125-128.

equations for mass transfer as:

$$\frac{\partial}{\partial t} [\rho_l (1 - \alpha)] + \frac{1}{A} \frac{\partial}{\partial z} [\rho_l (1 - \alpha) \bar{u}_l A] = -\Gamma \quad (2.25)$$

$$\frac{\partial}{\partial t} [\rho_g \alpha] + \frac{1}{A} \frac{\partial}{\partial z} [\rho_g \alpha \bar{u}_g A] = \Gamma \quad (2.26)$$

The area average void fraction is represented by  $\alpha$ ,  $\rho$  is the phase density,  $A$  is the channel cross-sectional area,  $\bar{u}$  is the average phase velocity, and  $\Gamma$  is the mass transfer rate per unit volume at the interface.

For momentum transfer, Levy gives the following general equations:

$$\begin{aligned} \frac{\partial}{\partial t} [\rho_l (1 - \alpha) \bar{u}_l] + \frac{1}{A} \frac{\partial}{\partial z} [\rho_l (1 - \alpha) \bar{u}_l^2 A] = & - (1 - \alpha) \frac{\partial p}{\partial z} - g \rho_l (1 - \alpha) \sin \theta \\ & - \frac{P_{wl} \tau_{wl}}{A} + \frac{P_i \tau_i}{A} + \Gamma \bar{u}_{il} \\ & + C \alpha \bar{\rho} (1 - \alpha) \frac{\partial (\bar{u}_g - \bar{u}_l)}{\partial t} \end{aligned} \quad (2.27)$$

$$\begin{aligned} \frac{\partial}{\partial t} (\rho_g \alpha \bar{u}_g) + \frac{1}{A} \frac{\partial}{\partial z} (\rho_g \alpha \bar{u}_g^2 A) = & - \alpha \frac{\partial p}{\partial z} - g \rho_g \alpha \sin \theta - \frac{P_{wg} \tau_{wg}}{A} \\ & - \frac{P_i \tau_i}{A} + \Gamma \bar{u}_{ig} - C \alpha \bar{\rho} (1 - \alpha) \frac{\partial (\bar{u}_g - \bar{u}_l)}{\partial t} \end{aligned} \quad (2.28)$$

The right sides of these equations represent the various forces applied to each phase. The first term is the net pressure force, and the second term is the gravitational force. The third term is the wall frictional force, or wall shear, and the fourth term is the interfacial frictional force, or interfacial shear. The phasic wetted perimeter is represented by  $P_i$ , and  $\frac{P_i}{A}$  represents the interfacial area per unit volume, interfacial area concentration. The fifth term is the momentum transferred at the interface by mass exchange between the phases. The final term is the virtual mass term, and represents the force required to accelerate the mass of the surrounding phase, when the relative velocity changes.

$C$  is a constant that depends on flow regime, and  $\bar{\rho}$  is the average mixture density,  $\bar{\rho} = \rho_g \alpha + \rho_l (1 - \alpha)$ .

The TRAC-M code neglects the virtual mass term in the momentum equations. The virtual mass term only becomes significant in very highly changing flow velocities, such as critical flow. TRAC-M also assumes that the interfacial velocity can be approximated as the difference between average phase velocities. In contrast, Collier<sup>24</sup> assumes that the mass transferred across the interface is accelerated to the mean velocity of the receiving phase, and therefore uses the associated average phase velocity in place of the interfacial velocity in the momentum mass transfer term. The determination of the true interfacial velocity will be one parameter for which NMR could be ideally suited.

For energy conservation, we will only present the gas phasic field equations, as the liquid phase equations are similar. Levy gives:

$$\frac{\partial}{\partial t} (\rho_g \alpha \bar{h}_g^o) + \frac{1}{A} \frac{\partial}{\partial z} (\rho_g \alpha \bar{h}_g^o \bar{u}_g A) = q_g''' \alpha + \frac{q_{ig}'' P_i}{A} + \frac{q_{wg}'' P_{hg}}{A} + \Gamma \bar{h}_{ig}^o + \alpha \frac{\partial P}{\partial t} + \xi \frac{P_i}{A} \tau_i \bar{u}_{ig} \bar{h}_g^o \quad (2.29)$$

The total gas phase enthalpy is given by  $\bar{h}_g^o$ . The first term on the right side is the heat generation in the gas, and the second term represents the interfacial heat flux into the gas phase. The third term is the wall heat flux into the gas phase, and the fourth term accounts for energy addition into the phase due to mass transfer at the interface. The fifth term accounts for work due to expansion or contraction of the phase, and the last term accounts for frictional dissipation at the interface.

TRAC-M adapts a different form for the energy equations, and uses internal energy,  $e$ , versus enthalpy,  $h$ . TRAC-M provides one equation for the gas phase, and then uses another equation for the combined gas and liquid phases, instead of an equation for the liquid phase only. This approach removes the interface to liquid dependence of the

---

<sup>24</sup> J.G. Collier, **Convective Boiling and Condensation**, Third edition, Clarendon Press, 1994, pp. 34-41.

model. For TRAC-M, the applicable one-dimensional gas phase equation is:

$$\frac{\partial}{\partial t} (\alpha \rho_g e_g) + \frac{\partial}{\partial z} (\alpha \rho_g e_g \bar{u}_g) = -P \frac{\partial \alpha}{\partial t} - P \frac{\partial}{\partial z} (\alpha \bar{u}_g) + q_{wg} + q_{ig} + q_{dg} + q_{gl} + \Gamma h'_v \quad (2.30)$$

The heat transfer terms on the left side of the equation are the wall-to-gas,  $q_{wg}$ , interface-to-gas,  $q_{ig}$ , heat deposited directly in the gas,  $q_{dg}$ , and the liquid-to-gas sensible heat transfer,  $q_{gl}$ . The interfacial terms are important for this chapter, and will be briefly discussed. The interface-to-gas term is given by

$$q_{ig} = h_{ig} a_i \frac{(T_g - T_{sat})}{V_{cell}} \quad (2.31)$$

where  $h_{ig}$  is the associated heat transfer coefficient,  $a_i = \frac{P_i}{A}$  is the interfacial area concentration,  $T_g$  is the gas phase temperature,  $T_{sat}$  is the saturation temperature, and  $V_{cell}$  is the cell volume. Note that the interfacial area concentration is required for proper closure. In addition, the sensible heat transfer is given by,

$$q_{gl} = h_{gl} a_i \frac{(T_g - T_l)}{V_{cell}} \quad (2.32)$$

which again incorporates the interfacial area concentration.

A very important closure parameter for all field equations is  $\Gamma$ , the rate of interfacial mass transfer.  $\Gamma$  is negative for mass transfer to the liquid, and positive for mass transfer to the gas.  $\Gamma$  depends on four other closure parameters:

- $a_i$ , the interfacial area concentration
- $h_{il}$ , the interface to liquid heat transfer coefficient
- $h_{ig}$ , the interface to gas heat transfer coefficient
- $h_{wl}$ , the wall to liquid heat transfer coefficient

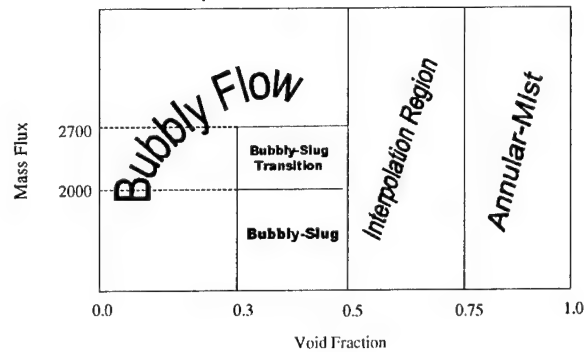


Figure 2-4: Flow regimes defined in the TRAC-M code.

### 2.3.3 Interfacial Area

One of the most significant closure variables for the two-fluid models described in the previous section is the interfacial area concentration. It plays a role in all interfacial terms, notably the interfacial mass transfer,  $\Gamma$ , interfacial shear,  $a_i \tau_i$ , and interfacial heat transfer,  $q_{ig} = q''_{ig} a_i$ . It is customary to define relationships for the interfacial area based on flow regime and its corresponding geometry, particularly the characteristic length scales of the system (such as bubble diameter). For example, Figure (2-4) shows the flow regimes used in the TRAC-M code. The particular regime is dependent on the total mass flux, and the calculated void fraction in the particular cell. Based on location within this map, the interfacial area calculation is determined using geometrical considerations and previously developed correlations. For example, in the bubbly flow regime, TRAC-M<sup>25</sup> uses

$$a_i = \frac{6\alpha}{D_b} \quad (2.33)$$

<sup>25</sup>TRAC-M/FORTRAN 90 (VERSION 3.0) **Theory Manual**, J. W. Spore et al., U.S. NRC, July 2000, p. F-12.

where  $D_b$  is the Sauter mean diameter of the bubbles<sup>26</sup>

$$D_b = \frac{\sum_j \left( \frac{6V_j}{\pi} \right)}{\sum_j \left( \frac{A_j}{\pi} \right)} \quad (2.34)$$

where the sums are taken over the number of bubbles. Eqn. (2.33) is based purely on geometry and the definition of  $D_b$ . TRAC-M determines  $D_b$  based on a suggestion by Ishii<sup>27</sup>

$$D_b = 2L_o \quad (2.35)$$

where  $L_o$  is the Laplace number defined as

$$L_o = \sqrt{\frac{\sigma}{g(\rho_l - \rho_g)}} \quad (2.36)$$

The bubble diameter  $D_b$  obtained in Eqn. (2.35) is an approximate arithmetic average. Using these methods, the Sauter mean diameter in the bubbly flow regime is a weak function of pressure. Thus, the interfacial area is simply determined by Eqn. (2.33) and is only strongly dependent on the void fraction and a relatively constant bubble size, or basically the number of bubbles of a constant radius. These types of calculations are typical of those used for many flow regimes in several computer codes. TRAC-M code writers readily admit that this type of calculation is rough and possibly inaccurate, but it is sufficient to meet code evaluation requirements when compared to experimental data (i.e., code validation).

Levy<sup>28</sup> discusses a method used by several investigators and computer codes that uses

---

<sup>26</sup>Levy, S., **Two-Phase Flow in Complex Systems**, John Wiley and Sons, Inc., 1999, pp.177-178.

<sup>27</sup>M. Ishii, Argonne National Laboratory, Private Communication, Letter to R. Nelson, Los Alamos National Laboratory, (July 1987).

<sup>28</sup>Levy, S., **Two-Phase Flow in Complex Systems**, John Wiley and Sons, Inc., 1999, pp.132-133, 177-178.

a critical Weber number in the calculation of the mean bubble diameter. The critical weber number, given by

$$Wb = \frac{D_{b,\max} \rho_l (\overline{u_g - u_l})^2}{\sigma} \quad (2.37)$$

is representative of the maximum bubble diameter in a two-phase system. The codes assume a Weber number (10 is often used), and then calculate  $D_{b,\max}$ . Assuming a distribution of sizes,  $D_b$ , is determined (often,  $D_{b,\max}$  is taken to be  $2D_b$ ). Therefore, as the relative velocity between the phases increases, this method would determine that  $D_b$  decreases. In actuality, as determined by photographic and ultrasonic methods, and pointed out by Levy, the bubble diameter increases because of a grouping effect.

The development of an interfacial area transport equation is being researched by a team at Purdue University under the guidance of Ishii. The addition of this equation will help alleviate many of the problems associated with current methods, including jump discontinuities at flow regime transitions, and trend problems.

NMR can possibly shed light onto the behavior of the interfacial area in two-phase systems. This thesis will investigate and develop the physics associated with using the dipolar field to determine interfacial area in a static two-phase system. Specifically, the dipolar field can be used to get a very good estimate of the characteristic length scale of a system (for example, average bubble diameter). In addition, using established techniques, NMR is well suited for measuring the volume fraction of each species present. A combination of the two measurements, together with a model of the size distribution, should give a good estimate of the interfacial area in the sample.

### 2.3.4 Interfacial Velocity and Shear

Interfacial shear plays a significant role in the momentum transfer equations, Eqns. (2.27) and (2.28). The term,  $\frac{P_{Ti}}{A}$ , which combines the interfacial area and the shear stress, enters into each equation, and is a significant contribution to the pressure drop in two



phase forced convection. In addition, the interfacial velocity enters into the momentum equations as  $\Gamma \bar{u}_{il}$  and  $\Gamma \bar{u}_{ig}$ . These terms represent the momentum transfer caused by mass transfer at the interface. As discussed before, these terms are often approximated by the bulk velocities of the receiving phase or the difference between the bulk velocities of the two phases.

The accepted definition for wall shear stress is given by

$$\tau_w = \mu \frac{\partial u}{\partial y} \Big|_{y=0} \quad (2.38)$$

where  $y$  is perpendicular distance from the wall, and  $u$  is the fluid velocity along the wall. A similar expression can be used to describe the interfacial shear stress for each phase.

$$\tau_i = \mu \frac{\partial u}{\partial y} \Big|_{y=\text{interface}} \quad (2.39)$$

Basically, the interfacial shear is the slope of the velocity profile at the interface. This stress will differ between phases because of different viscosities and velocity profiles. Thus, if the phasic velocities can be measured at given distances from the interface, the resulting distribution can be plotted and the slopes at the interface determined. However, this method of shear stress determination is not used in practice because of the difficulties with experimentally measuring interfacial velocities in this fashion.

Typically, interfacial shear is incorporated into computer codes using developed correlations and estimations of interfacial friction factors. Shear stress is given by equations of the type

$$\tau_i = \rho_t \frac{C_D}{8} (\bar{u}_r) |\bar{u}_r| \quad (2.40)$$

where  $C_D$  is the interfacial drag coefficient and  $\bar{u}_r$  is the average relative velocity between

the phases. Usually,  $\bar{u}_r$  is simplified by

$$\bar{u}_r = \overline{u_g - u_l} \approx \bar{u}_g - \bar{u}_l \quad (2.41)$$

This equation is only valid for radially uniform velocity and void profiles, but is still widely used in practice. For example, the TRAC-M code the interfacial shear term takes the form

$$\frac{P_i \tau_i}{A} = c_i (\vec{u}_g - \vec{u}_l) |\vec{u}_g - \vec{u}_l| \quad (2.42)$$

where the velocities are the average phasic velocities in the node, and  $c_i$  is the interfacial drag coefficient and depends on flow regime. For bubbly flow

$$c_i = \frac{3c_{Db}\alpha_l P_s}{4D_b} \quad (2.43)$$

where  $c_{Db}$  is the bubble drag coefficient and is a function of a bubble Reynold's number,  $D_b$  is the bubble diameter that is a function of the Laplace number, and  $P_s$  is a profile slip factor that accounts for migration of bubbles into the region of the flow channel with higher velocity.

The use of the dipolar field in NMR offers an opportunity to further explain interfacial shear in two-phase systems. As will be explained in Chapter 3, the distance of the dipolar field interaction between two phases is directly under experimental control. Conceivably, by systematically adjusting this distance, and then measuring the velocity of the spins within this distance, the velocity distribution at the interface could be investigated. Chapter 4 will further explore the physics associated with the NMR signal behavior for such an experiment.

## Chapter 3

# Signal Physics

The dipolar field effect is well known in the field of NMR, especially in the context of solid state NMR<sup>1</sup>. In liquids, the dipolar field is often neglected because of diffusion and motional narrowing. In recent years, interest has been generated in the reintroduction of dipolar effects in liquids. With improvements in magnetic field and NMR technology, along with a better understanding of the physics behind dipolar effects in liquids, the examination and use of these effects for NMR spectroscopy and imaging techniques has risen dramatically in the last decade.

Deville<sup>2</sup> observed a dipolar field in He-3 where a relatively strong external gradient created a magnetization grating and thus a local macroscopic dipolar field. The NMR signal then resulted from the evolution of the system in the presence of the magnetization grating and dipolar field to generate nonlinear effects and multiple echoes. Warren et al.<sup>3</sup> suggested that the dipolar field could be used to investigate structural properties of liquid NMR samples, and that the effective length over which the field interacts is mostly limited to within one-half wavelength of the applied gradient pitch. Structural properties have

---

<sup>1</sup>C.P.Slichter, **Principles of Magnetic Resonance**, Third Edition, Springer-Verlag Berlin Heidelberg, 1990.

<sup>2</sup>G. Deville, M. Bernier, J. M. Delrieux, "NMR Multiple Echoes Observed in Solid He-3", *Physical Review B*, Vol. 19, Number 11, 1 June 1979, pp. 5666-5688.

<sup>3</sup>Warren S. Warren, Wolfgang Richter, et al., "Generation of Impossible Cross Peaks Between Bulk Water and Biomolecules in Solution NMR", *Science*, Vol. 262, 24 December 1993, pp. 2005-2009.

Experiment	Applicable Equation
Imaging	$i(\vec{k}) = \int \rho(\vec{r}) e^{i\vec{k} \cdot \vec{r}} d\vec{r}$
Scattering	$s(\vec{q}, t) = \int \rho(\vec{r}) e^{i\vec{q} \cdot \vec{r}} \int P(\vec{r} \vec{r}') e^{-i\vec{q} \cdot \vec{r}'} d\vec{r}' d\vec{r}$
Mean Field	$d(\vec{q}, t) = \int \rho(\vec{r}) e^{i\vec{q} \cdot \vec{r}} e^{-i\gamma t \frac{\mu_0}{4\pi} \int \frac{\rho_{source}(\vec{r}') A(\vec{r}') (3 \cos^2 \theta_{\vec{r}\vec{r}'} - 1)}{ \vec{r} - \vec{r}' ^3} d\vec{r}'} d\vec{r}$

Table 3.1: Comparison of three NMR experiments used for size determination

since been examined by Bowtell for simple cylindrical geometries<sup>4</sup>, periodic geometries<sup>5</sup>, and randomly packed microspheres<sup>6</sup>. Bowtell also described how the dipolar field could be used to measure the spatial auto-correlation function (or Patterson function) of the magnetization in the system<sup>7</sup>.

The present study focuses on using the dipolar field to investigate structural properties of a relatively complex system. Specifically, we show that Dipolar Demagnetizing Field (DDF) experiments can be used to complement existing Nuclear Magnetic Resonance (NMR) techniques for investigating structural properties of two-phase systems. Table (3.1) illustrates the complementary nature of DDF experiments compared to imaging and normal scattering experiments (neglecting relaxation). In Table (3.1),  $\rho$  is the spin density, while  $\vec{q}$  and  $\vec{k}$  are wave vectors.

The imaging signal,  $i(\vec{k})$ , provides a measure of the absolute position of spins by phase encoding their location in the form of a magnetization grating<sup>8</sup>. The spatial resolution is largely limited by gradient strength and diffusion. Scattering is concerned with spin displacements<sup>9</sup>. Scattering experiments give a measure of the conditional

<sup>4</sup>R. Bowtell, P. Robyr, "Structural Investigations with the Dipolar Demagnetizing Field in Solution NMR", *Physical Review Letters*, Vol. 76, No. 26, 24 June 1996, pp.4971-4974.

<sup>5</sup>P. Robyr, R. Bowtell, "Nuclear Magnetic Resonance Microscopy in Liquids Using the Dipolar Field", *Journal of Chemical Physics*, Vol. 106 (2), 8 January 1997, pp. 467-476.

<sup>6</sup>P. Robyr, R. Bowtell, "Measuring Patterson Functions of Inhomogeneous Liquids Using the Nuclear Dipolar Field", *Journal of Chemical Physics*, Vol. 107 (3), 15 July 1997, pp. 702-706.

<sup>7</sup>Ibid., p.703.

<sup>8</sup>A. Sodickson and D.G. Cory, "A Generalized k-space Formalism for Treating the Spatial Aspects of a Variety of NMR Experiments", *Progress in Nuclear Magnetic Resonance Spectroscopy*, **33** (1998), pp. 77-108.

<sup>9</sup>P.T. Callaghan, **Principles of Nuclear Magnetic Resonance Microscopy**, Oxford University Press, Inc., New York, 1995.

displacement probability over a given time scale. In Table (3.1),  $s(\vec{q}, t)$  is the signal intensity, and  $P(\vec{r}|\vec{r}')$  is the conditional displacement probability for spin at position  $\vec{r}$  to move to position  $\vec{r}'$  during time,  $t$ . Scattering experiments are dynamic in nature, and the cleanest structural measurements are made in the limit of bounded diffusion<sup>10</sup>. Thus, scattering experiments are limited to length scales below about  $50\mu\text{m}$ .

The inter-species DDF provides a magnetic field at the location of one species resulting from the magnetization distribution of another species. The mean field equation in Table (3.1) gives the secular DDF resulting from a  $z$ -axis source magnetization distribution. The DDF contributes a phase to the observed spins.  $d(\vec{q}, t)$  is the signal resulting from the mean DDF,  $\rho_{\text{source}}(\vec{r}')$  is the spin density of the source spins, and  $A(\vec{r}')$  is a function that represents this distribution of source magnetization, which depends on preparation methods in the applicable pulse sequence. The applied gradient  $e^{i\vec{q}\cdot\vec{r}}$  term acts to filter out structural information contained in spatial Fourier components of the correlated spins. The extent of the spatial cross-correlation is limited by diffusion and the range over which the field interacts. The technique is well suited for studying systems with large length scales.

The present work focuses on introducing a methodology that can be used to study complex systems with DDF scattering experiments. The system under study is a poly-disperse oil/water emulsion, created by dispersing oil bubbles in an aqueous agarose gel. Specifically, the DDF can be used to determine the average oil droplet size and some measure of the overall bubble size distribution.

### 3.1 Theory

This section discusses the theoretical derivation of the NMR signal generated from the dipolar demagnetizing field in a sample of immiscible oil bubbles emulsified within a water phase. The pulse sequence is designed such that the signal results from the mean

---

<sup>10</sup>D.G. Cory and A.N. Garroway, *Mag. Reson., Med.*, **14**, 435.

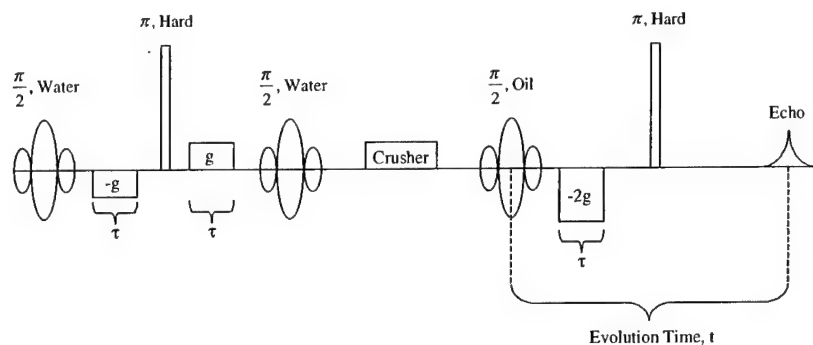


Figure 3-1: Pulse sequence for emulsion experiment.

field dipolar interaction between the water and the oil, and carries information on the sample geometry, including the bubble size.

### 3.1.1 Basic Experiment and Overview

The experiment is shown schematically in Figure (3-1). It is essentially a stimulated echo with a transfer of spatial coding from water to oil during the storage period. The gradient between the two water  $\frac{\pi}{2}$  pulses generates a sinusoidally modulated magnetization in the water along the  $z$ , or  $B_0$ , direction. Spatial information is exchanged between the water and oil through the mean field dipolar interaction. This method is very similar to those studied by Warren<sup>11</sup> and Bowtell<sup>12</sup> for structural measurements.

During the mixing time, the water's longitudinal magnetization is represented by the following equation:

$$\vec{M}_{water} = M_{o,water} \cos(q_m z + q_m \delta) \hat{z} \quad (3.1)$$

where:

<sup>11</sup>Warren S. Warren, Wolfgang Richter, et al., "Generation of Impossible Cross Peaks Between Bulk Water and Biomolecules in Solution NMR", *Science*, Vol. 262, 24 December 1993, pp. 2005-2009.

<sup>12</sup>R. Bowtell, P. Robyr, "Structural Investigations with the Dipolar Demagnetizing Field in Solution NMR", *Physical Review Letters*, Vol. 76, No. 26, 24 June 1996, pp.4971-4974.

- $M_{o,water}$  is the water equilibrium magnetization.
- $q_m = \gamma g \tau$  is the spatial wave number of the grating,  $g$  is the magnitude of the gradient pulse, and  $\tau$  is the duration of the gradient pulse. The wavelength (or pitch) of the grating is  $\lambda = \frac{2\pi}{q_m}$ .
- $\delta$  is the position offset of the magnetization grating, which depends on the r.f. pulse phase.

### 3.1.2 Calculation of the Magnetic Field in an Oil Bubble

From a known geometry of the two phases, the mean field of the water seen by a test oil spin is straightforwardly calculated from the spatially distributed water dipoles<sup>13</sup>,

$$B_d(\vec{r}) = \int \frac{d^3 r'}{|\vec{r} - \vec{r}'|^3} \left\{ \vec{M}_{water}(\vec{r}') - \frac{3 \left[ \vec{M}_{water}(\vec{r}') \cdot (\vec{r} - \vec{r}') \right] (\vec{r} - \vec{r}')}{|\vec{r} - \vec{r}'|^2} \right\} \quad (3.2)$$

Deville et al.<sup>14</sup> used a Fourier transformed form of Eqn. (3.2) to derive a local form of the field that did not depend on structural properties, and Bowtell et al.<sup>15</sup> Fourier transformed the field and equilibrium magnetization distribution to solve the associated NMR signal problem in spatial Fourier space. In the present research it is more consistent to explore the mean field for the specific geometry of distributed spheres.

We start by calculating the field within a single sphere located in a static magnetism grating of infinite spatial extent. The water surrounds a single spherical oil bubble of radius  $a$ . The water magnetization distribution is approximated as a ferromagnet with zero macroscopic current density,  $\vec{J} = 0$ .

<sup>13</sup>G. Deville, M. Bernier, J. M. Delrieux, "NMR Multiple Echoes Observed in Solid He-3", *Physical Review B*, Vol. 19, Number 11, 1 June 1979, pp. 5666-5688.

<sup>14</sup>Ibid., p. 5667.

<sup>15</sup>R. Bowtell, P. Robyr, "Structural Investigations with the Dipolar Demagnetizing Field in Solution NMR", *Physical Review Letters*, Vol. 76, No. 26, 24 June 1996, pp.4971-4974.

We proceed by finding the scalar magnetic potential,  $\Phi$ , and then the magnetic field intensity,  $\vec{H} = -\nabla\Phi$ , is calculated from the spatial gradient of the potential. Finally, the magnetic flux density,  $\vec{B}_{oil}$ , is determined,

$$\vec{B}_{oil} = \mu_o(\vec{H}_{oil} + \vec{M}_{oil}) \quad (3.3)$$

$\vec{B}$  is the magnetic flux density (sometimes called the magnetic induction).  $\mu_o$  is the permeability of free space,  $\mu_o = 4\pi \times 10^{-7} (\frac{Wb}{A \cdot m})$ . The internal field derivation neglects the small change in the permeability between the oil and water. The associated effects on the internal field are small. However, permeability differences will contribute a significant "susceptibility field" in the water. This effect will be discussed later.

The solution to Poisson's equation<sup>16</sup>,

$$\nabla^2\Phi = \nabla \cdot \vec{M}, \quad (3.4)$$

with boundary surfaces is,

$$\Phi = -\frac{1}{4\pi} \int \frac{\nabla' \cdot \vec{M}(\vec{r}')}{|\vec{r} - \vec{r}'|} d^3r' + \frac{1}{4\pi} \oint \frac{\hat{n}' \cdot \vec{M}(\vec{r}')}{|\vec{r} - \vec{r}'|} da' \quad (3.5)$$

The prime coordinates indicate the source coordinates (water), and the unprimed coordinates indicate the location for observation of the potential (oil).  $\hat{n}'$  is the unit normal to the surface ( $\hat{n}' = \hat{r}'$ ), and  $da'$  is an element of surface area on the boundary of the sphere. To calculate the potential, we first solve the potential equation for a sphere of radius  $R$  of the given water magnetization. Then, from this potential, we subtract the potential of a sphere of water that is the size of the oil bubble, radius  $a$ . The resulting potential is that which exists within a "hollowed-out" sphere located within the water magnetization. See Figure (3-2).

The coordinate system for this calculation is centered at the center of the oil sphere

---

<sup>16</sup> John D. Jackson, **Classical Electrodynamics**, John Wiley and Sons, Inc., Third Edition, 1999.



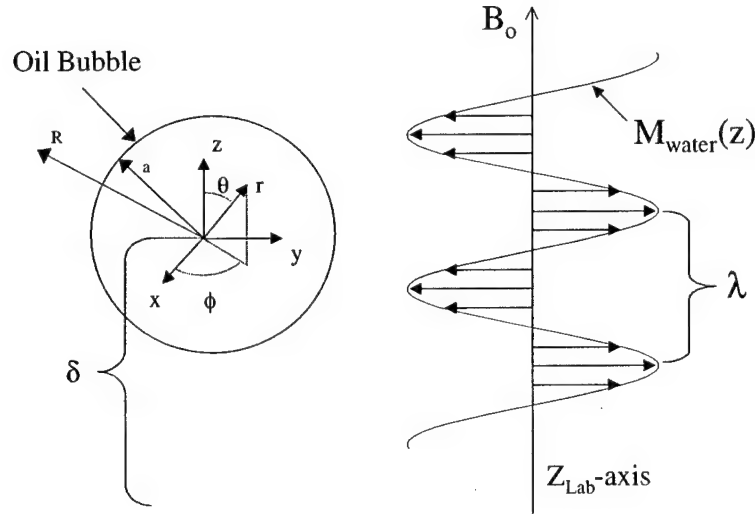


Figure 3-2: Coordinate system and problem setup for the mean field calculation.

with radial coordinate,  $r$ . Therefore, “ $z$ ” in Eqn.(3.1) is the longitudinal coordinate within the bubble, and  $\delta$  is the position offset of the magnetization at the origin of this coordinate system. The offset in this coordinate system will depend on the phase of the r.f.pulses, and also on the bubble’s location along the longitudinal axis of the sample.

The divergence of the magnetization is

$$\nabla' \cdot \vec{M}(\vec{r}') = -M_{o,water} q_m \sin(q_m z' + q_m \delta) \quad (3.6)$$

and the component of the magnetization along  $\hat{r}'$  is

$$\hat{r}' \cdot \vec{M}(\vec{r}') = M_{o,water} \cos(q_m z' + q_m \delta) \cos(\theta') \quad (3.7)$$

In spherical coordinates for a sphere of radius  $R$ , Eqn.(3.5) is,

$$\begin{aligned}\Phi_R = & -\frac{1}{4\pi} \int_{r'=0}^R \int_{\theta'=0}^{\pi} \int_{\phi'=0}^{2\pi} \frac{-M_{o,water} q_m \sin [q_m r' \cos(\theta') + q_m \delta]}{|\vec{r} - \vec{r}'|} r'^2 \sin(\theta') dr' d\theta' d\phi' \\ & + \frac{1}{4\pi} \int_{\theta'=0}^{\pi} \int_{\phi'=0}^{2\pi} \frac{M_{o,water} \cos [q_m R \cos(\theta') + q_m \delta] \cos(\theta')}{|\vec{r} - \vec{r}'|} R^2 \sin(\theta') d\theta' d\phi'\end{aligned}\quad (3.8)$$

The term  $\frac{1}{|\vec{r} - \vec{r}'|}$  (the Green's function) can be expanded into the following<sup>17</sup>,

$$\frac{1}{|\vec{r} - \vec{r}'|} = 4\pi \sum_{l=0}^{\infty} \sum_{m=-l}^l \frac{1}{2l+1} \frac{r_{<}^l}{r_{>}^{l+1}} Y_{lm}^* [\theta', \phi'] Y_{lm} [\theta, \phi] \quad (3.9)$$

This expansion gives the potential at  $\vec{r}$  due to the magnetization at  $\vec{r}'$ .  $Y_{lm} [\theta, \phi]$  is the spherical harmonic. The radial parameters,  $r_{<}$  and  $r_{>}$ , represent the smaller and larger of  $r$  and  $r'$  respectively. Given the azimuthal symmetry of our spherical problem (the water magnetization only depends on the  $z$  coordinate), this expansion can be simplified by setting  $m = 0$  and using Legendre polynomials,  $P_l$ , instead of spherical harmonics,

$$Y_{l0} = \sqrt{\frac{2l+1}{4\pi}} P_l [\cos(\theta)] \quad (3.10)$$

and the overall expansion simplifies to,

$$\frac{1}{|\vec{r} - \vec{r}'|} = \sum_{l=0}^{\infty} \frac{r_{<}^l}{r_{>}^{l+1}} P_l [\cos(\theta')] P_l [\cos(\theta)] \quad (3.11)$$

Following the above substitutions, subtracting an equivalent expression with a smaller spherical boundary of radius  $a$ , and integrating over  $\phi'$ , the potential inside the inner

---

<sup>17</sup> John D. Jackson, **Classical Electrodynamics**, John Wiley and Sons, Inc., Third Edition, 1999.

sphere is,

$$\begin{aligned}
\Phi = \Phi_R - \Phi_a = & -\frac{1}{4\pi} \int_{r'=a}^R \int_{\theta'=0}^{\pi} \{-2\pi M_{o,water} q_m \sin[q_m r' \cos(\theta') + q_m \delta] r'^2 \sin(\theta') dr' d\theta' \\
& \times \sum_{l=0}^{\infty} \frac{r'^l}{r'^{(l+1)}} P_l[\cos(\theta')] P_l[\cos(\theta)]\} \\
& + \frac{1}{4\pi} \int_{\theta'=0}^{\pi} \{2\pi M_{o,water} \cos[q_m R \cos(\theta') + q_m \delta] \cos(\theta') R^2 \sin(\theta') d\theta' \\
& \times \sum_{l=0}^{\infty} \frac{r'^l}{R^{(l+1)}} P_l[\cos(\theta')] P_l[\cos(\theta)]\} \\
& - \frac{1}{4\pi} \int_{\theta'=0}^{\pi} \{2\pi M_{o,water} \cos[q_m a \cos(\theta') + q_m \delta] \cos(\theta') a^2 \sin(\theta') d\theta' \\
& \times \sum_{l=0}^{\infty} \frac{r'^l}{a^{(l+1)}} P_l[\cos(\theta')] P_l[\cos(\theta)]\}
\end{aligned} \tag{3.12}$$

It is convenient to introduce a new dimensionless parameter called the size ratio,  $\Lambda_{q_m}$ , describing the ratio of the sphere radius to the grating's period,

$$\Lambda_{q_m} = \frac{a * q_m}{2\pi} \tag{3.13}$$

The potential was computed using *Mathematica*. For  $\Lambda_{q_m} \leq .6$ , the potential is well described for  $l \leq 7$ . Higher  $\Lambda_{q_m}$  requires additional harmonics, and for our purposes  $l \leq 11$  suffices.

The flux density inside the bubble due to the water magnetization outside the bubble is,

$$\vec{B}_{oil}(r, \theta, \delta) = B_{oil,r}(r, \theta, \delta) \hat{r} + B_{oil,\theta}(r, \theta, \delta) \hat{\theta} \tag{3.14}$$

Only the  $z$ -component of the magnetic field leads to a variation in the oil precession rate. The  $z$ -component of the field is the projection of the spherical components of the

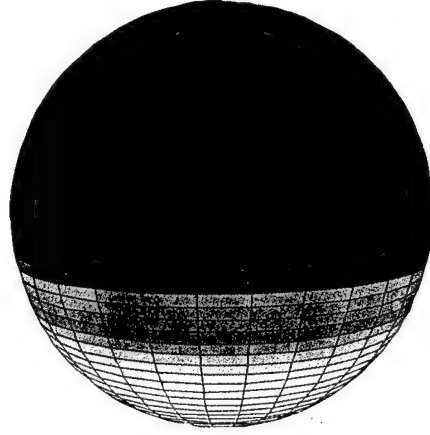


Figure 3-3: Parametric plot of the field intensity within an oil bubble ( $\Lambda_{q_m} = .5$ ,  $q_m\delta = \frac{2\pi}{3}$ )

$B$  vector on to the  $z$ -axis,

$$B_{oil,z}(r, \theta, \delta) = B_{oil,r}(r, \theta, \delta) \cos(\theta) - B_{oil,\theta}(r, \theta, \delta) \sin(\theta) \quad (3.15)$$

A visual example of the field calculation is shown in Figure (3-3). This figure shows  $B_{oil,z}(r, \theta, \delta)$  for a bubble with  $M_{o,water} = .045380 \frac{\text{A}}{\text{m}}$  (600 MHz),  $\Lambda_{q_m} = .50$ , and  $q_m\delta = 2\pi/3$ . In the cut-away section, red represents the highest field intensity, and corresponds to a peak in the outer water grating. Light blue represents zero intensity. Note that the grating structure is passed into the bubble, and how the field falls off in the interior of the bubble.

The essential physics is contained in the field variation over the oil sphere.

- 1) At  $q_m = 0$ , there is no spatial modulation of the water magnetization, and zero field over the sphere. The  $q_m = 0$  case is singular and care must be taken since the field depends on the shape of the inner and outer surfaces.
- 2) For finite  $q_m$ , the field calculation converges at  $R \gg \frac{1}{q_m}$ .

- 3) The field shape at the surface of the sphere mimics the water grating.
- 4) For  $a > \frac{1}{q_m}$ , the field falls off in the interior of the oil. The distance over which the dipolar field interacts in the presence of a spatial modulation is on the order of one-half the pitch of the grating.
- 5) The boundary conditions were verified at the interface, and the normal component of the flux density and tangential component of the field intensity are continuous.

### 3.1.3 Calculation of the Magnetization in the Oil Bubble

Given the dipolar demagnetizing field specified at every point within the bubble, we are now in a position to calculate the transfer of the magnetization grating from water to the oil. In a cylindrical coordinate system with coordinates  $\rho$  and  $z$ , a transverse differential volume element of oil magnetization within the bubble acquires a phase as a result of the dipolar demagnetizing field from the water (the azimuthal symmetry of the problem negates any dependence on  $\phi$ ). The time evolution equation for the augmented transverse oil magnetization, neglecting relaxation and diffusion, is,

$$\frac{dM_{oil}^+(\rho, z, \delta)}{dt} = -i\gamma M_{oil}^+(\rho, z, \delta) B_{oil,z}(\rho, z, \delta) \quad (3.16)$$

$M_{oil}^+(\rho, z, \delta)$  represents the complex transverse oil magnetization.  $B_{oil,z}$  does not depend on time and the solution of this equation results in,

$$M_{oil}^+(\rho, z, \delta, t) = M_{o,oil} e^{(-i\gamma B_{oil,z}(\rho, z, \delta)t)} \quad (3.17)$$

$M_{o,oil}$  is the equilibrium water magnetization, and the time,  $t$ , represents the evolution time of the water magnetization in the presence of the water dipolar field.

The spatially varying phase of the oil magnetization was calculated via a numerical integration of the field from the water spins. So far, the analysis has considered bubbles of constant radius. A more realistic assumption is to assume that the bubble diameters

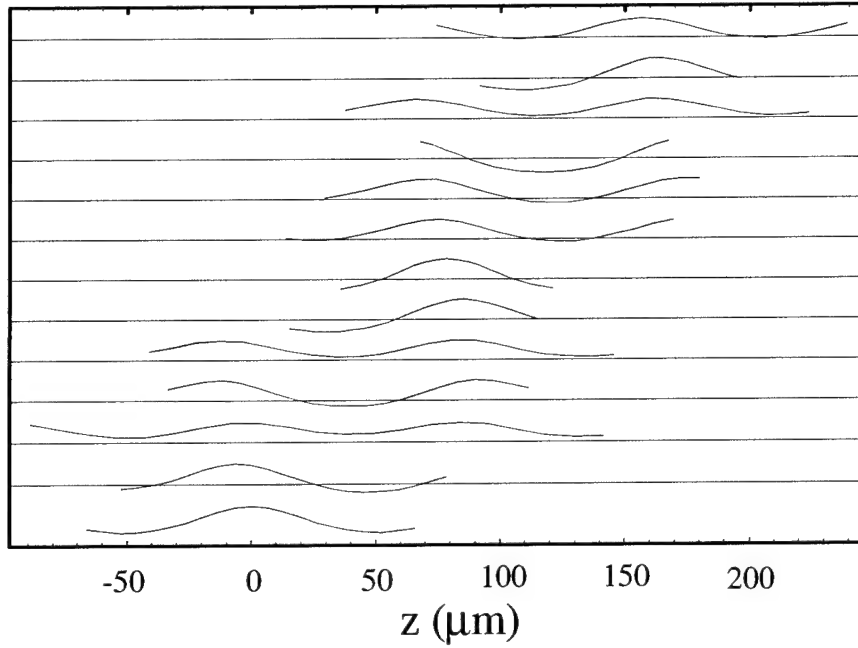


Figure 3-4: X-component of the oil magnetization versus  $z$

are distributed about a mean diameter,  $D_{mean}$ . This distribution is typically assumed to be log-normal for NMR diffusion studies<sup>18</sup>.

As shown in Table (1), the NMR signal results from the spatial Fourier transform of the oil magnetization throughout the sample. To perform the necessary integrations, we randomly choose a bubble size for each  $\delta$  location, perform the radial integration to determine  $M_{oil}^+(z, t, \delta)$  for each bubble, and then add up each bubble's contribution to the overall oil-magnetization in the sample to obtain  $M_{oil}^+(z_{Lab}, t)$ . This method projects the oil's radial magnetization on to the  $z_{Lab}$ -axis. Figure (3-4) gives a plot for the x-component (real part) of  $M_{oil}^+(z, t, \delta)$  for thirteen bubbles of varying sizes at different positions over one spatial wavelength. This simulation was calculated for  $D_{mean} = 165 \mu\text{m}$ ,  $q_m = 40 \text{ mm}^{-1}$ , and a dipolar evolution time of 300 ms. Our experiments were performed at a much shorter evolution time, but using a longer time for the figure clearly

<sup>18</sup>Olle Söderman, Balin Balinov, "NMR Self-Diffusion Studies of Emulsions", **Emulsions and Emulsion Stability** (edited by Johan Sjöblom), Surfactant Science Series Vol. 61, 1996, pp. 369-392.

shows the effects of the dipolar field. The resulting oil magnetization distributions will constructively interfere to give spatial harmonics of the water magnetization grating.

A Fourier transformation of the resulting oil magnetization over  $L$  provides Fourier components at integer multiples of the spatial wave number. We normalize this Fourier transform by dividing by the equilibrium oil magnetization to result in the following equation for the first spatial Fourier component,

$$Area\ Ratio = \frac{1}{M_{o,oil}L} \int_0^L M_{oil}^+(z_{Lab}, t) e^{-iq_m z_{Lab}} dz_{Lab} \quad (3.18)$$

where,

$$z_{Lab} = z + \delta \quad (3.19)$$

The normalization has the effect of removing the dependence of the signal ratio on the relaxation of the oil magnetization. This normalization is similar to Bowtell's normalization<sup>19</sup>, and it will simplify comparison of the calculations to the experimental results. We then plot the magnitude of the normalized first spatial Fourier component versus evolution time to generate buildup functions, see Figures (3-5) or (3-8).

The effects of the different permeabilities between the oil and the water are now considered. Because this difference is very small, it will have a very small effect on the field inside the bubble. For the field calculation, we have assumed the permeabilities to be equal. However, the small difference in permeability has a significant effect on the grating produced in the water because of a static "susceptibility field" present in the region surrounding the bubble. For a spherical geometry, the difference in permeability manifests itself by giving the sphere an "effective" uniform magnetization along the  $z$ -axis. This magnetization results in a uniform field within the sphere and a dipolar field surrounding the sphere. The susceptibility field tends to disturb the formation of the

---

<sup>19</sup>R. Bowtell, P. Robyr, "Structural Investigations with the Dipolar Demagnetizing Field in Solution NMR", *Physical Review Letters*, Vol. 76, No. 26, 24 June 1996, pp.4971-4974.

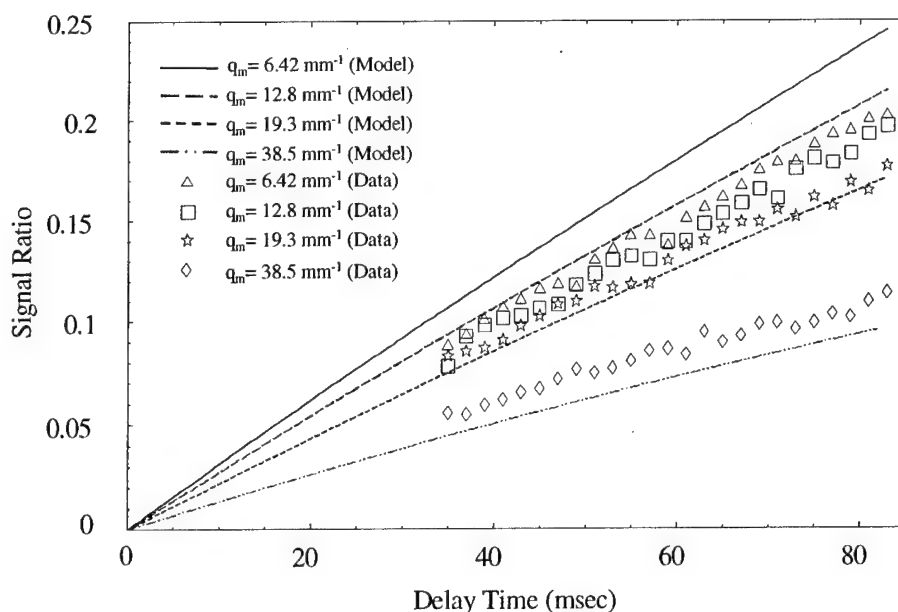


Figure 3-5: Comparison of experimental to model results ( $D_{mean} = 180\mu m$ )

water grating while the external gradient is applied as shown in Figure (3-6). This figure shows a simulation for the disruption of the water grating in an area close to the bubble for a bubble diameter of  $160\mu m$ , and a  $4.8\text{ G/cm}$  external gradient applied for  $1\text{ ms}$ . The disrupted area extends well out to  $30\mu m$  beyond the edge of the bubble. The susceptibility field can lead to attenuation of the signal. This is minimized following Lowe<sup>20</sup>, by adding a hard  $\pi$ -pulse to refocus spin evolution from time independent fields, while still writing a phase grating via the time dependence of the applied gradients. A hard  $\pi$ -pulse was also added after the oil selective pulse to refocus the effects of field inhomogeneities within the oil bubbles. Thus, the total evolution time for the dipolar demagnetizing field is from the center of the selective oil pulse until the formation of the echo after the  $\pi$ -pulse. The magnitude of the oil gradient is twice the magnitude of each of the water gradients in order to select the first Fourier component of the water's spatial

<sup>20</sup>R.F. Karlicek and I.J. Lowe, "A Modified Pulsed Gradient Technique for Measuring Diffusion in the Presence of Large Background Gradients", *Journal of Magnetic Resonance*, **37**, pp. 75-91 (1980).



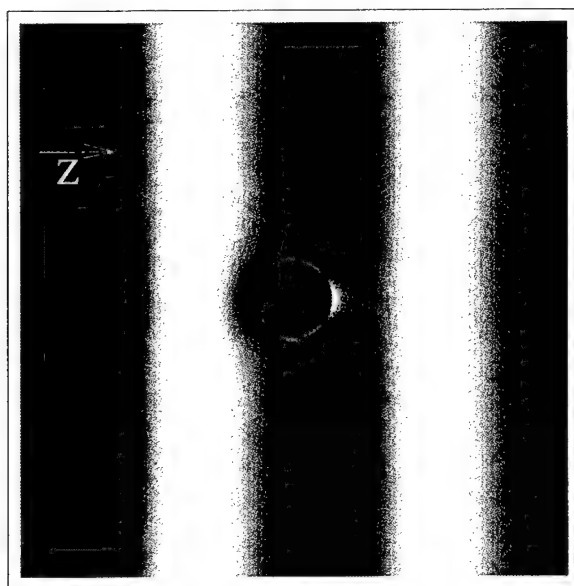


Figure 3-6: Susceptibility fields around an oil bubble.

modulation.

## 3.2 Experiments and Discussion

The emulsion was prepared from a 50/50% volume mixture of .02 *M* Sodium Dodecyl-Sulfate (SDS) and hexadecane. The oil/water mixture was shaken and then allowed to sit for a short time. After waiting, the creamed layer was removed, and this cycle was repeated several times<sup>21</sup>. The final creamed layer was transferred to a 5 mm NMR sample tube. Warm agarose solution (.05 *g* Agarose in 10 *ml* water) was added to the sample tube, which was gently agitated and cooled to suspend the oil bubbles in the gel. The final cooled sample consisted of separate oil bubbles surrounded by water. The mean diameter of the bubbles was visually estimated under a microscope to be approximately 150  $\mu\text{m}$  with bubble sizes ranging from about 25  $\mu\text{m}$  to 320  $\mu\text{m}$ .

<sup>21</sup>J. Bibette, "Depletion Interactions and Fractionated Crystallization for Polydisperse Emulsion Purification", *Journal of Colloid and Interface Science*, Vol. 147, No. 2, December 1991, pp. 474-478.

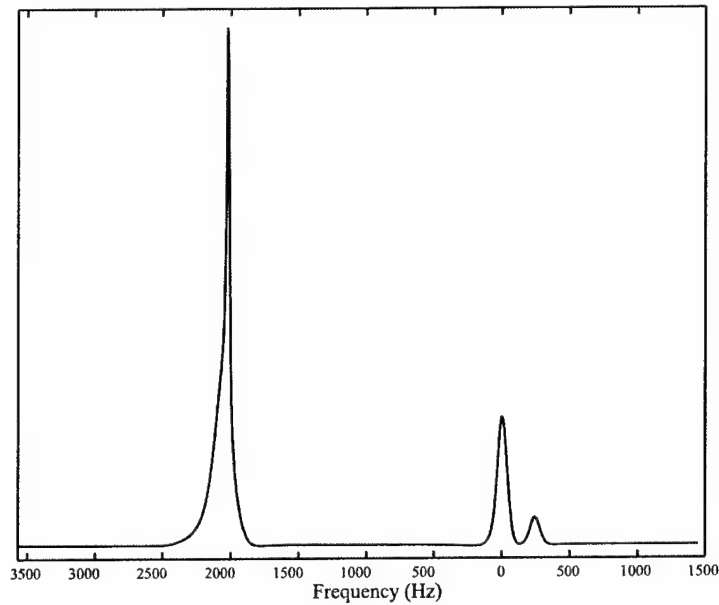


Figure 3-7: NMR spectrum of the emulsion sample.

The NMR experiments were performed on a Bruker AMX 600 MHz spectrometer. Figure (3-7) gives the one-dimensional NMR spectrum of the sample for a hard  $\pi/2$ -pulse on the methylene resonance. This figure shows how the water line is broadened at the base by the susceptibility fields near the oil bubbles. In fact, we can distinguish two “types” of water depending on its proximity to an oil bubble. The narrow peak seen at the top of the water spectrum is made up of water that is removed from the oil, and the broadened peak is made up of water that is close to the oil.

The sample’s relaxation times were:

- $T_{1water} = 2.81$  sec and  $T_{1oil} = 851$  sec
- $T_{2oil} = 48.8$  ms
- $T_{2water}^{short} = 29.3$  ms and  $T_{2water}^{long} = 76.2$  ms. The different water  $T_2$  values correspond to the different isochromats. The water close to the oil gives a lower  $T_2$  value because of diffusion through the susceptibility fields.

Experiments were conducted at four different  $q_m$  values ( $6.42\text{ mm}^{-1}$ ,  $12.8\text{ mm}^{-1}$ ,  $19.3\text{ mm}^{-1}$ , and  $38.5\text{ mm}^{-1}$ ). In each experiment the evolution time was varied from 35 to 83 msec. A spin echo experiment at the same delay times was used to normalize the dipolar experiments.

The buildup of the signal was simulated using the model presented in the previous section. The model accounts for unrestricted diffusion of the water, and  $T_2$  decay that occurs in the water while writing the grating.  $T_1$  relaxation of longitudinal magnetization was neglected.

The presence of the oil bubbles in the water disrupts the continuity of the water grating. In other words, for a given bubble, the water grating that surrounds the bubble will be interrupted by the presence of another bubble. To account for this effect, a volume fraction correction was included in the calculation of the water magnetization. The volume fraction was determined based on the ratio of the total oil NMR spectrum area to the total water spectrum area. By knowing the ratio of the water and oil spins in the sample, and knowing the molecular weights and densities of each species, we estimated the volume fraction,  $V_{frac} = \frac{V_{water}}{V_{total}}$ , of water as .760. This type of calculation is further explained in Chapter 4. This volume fraction correction factor was multiplied by the water magnetization in the model.

Figure (3-5) provides a comparison of the simulations to experimental results for a lognormal bubble diameter distribution with mean diameter of  $180\text{ }\mu\text{m}$  and standard deviation,  $\sigma$ , of  $75\text{ }\mu\text{m}$ . The magnitudes of the simulations closely match the experimental data for the higher  $q_m$  curves. The basic form of the simulations is the same as the experimental data, with a closer separation between the two lower  $q_m$  curves than the two higher  $q_m$  curves. The key feature of this data is the slope and relative slopes as  $q_m$  is varied. The vertical intercept is sensitive to diffusion and volume fraction considerations which are not interesting here.

Using the lower three values for  $q_m$  ( $q_m = 6.42, 12.8, 19.3\text{ mm}^{-1}$ ), the experimental results were compared to several simulations run with different average bubble sizes and

different size distributions, log-normal and Gaussian. The buildup function curves are approximately linear for the time frames of our experiments. Linear curves were fit to the experimental data and to the model curves in the time frames of the experiments, and the ratios of linear slopes between curves were compared to determine which set of model curves best matched the experimental data behavior. Based on the results, a log-normal distribution with a mean bubble diameter between  $140 - 160 \mu\text{m}$  was chosen as having the best fit. Smaller diameter bubbles show groupings that are close together relative to the data, and larger diameter bubbles show groupings that are spaced further apart. These results match well with the observed average bubble size of  $150 \mu\text{m}$ . The Gaussian curves did not match the behavior of the data quite as well as the log-normal curves (the curves at low  $q_m$  were not grouped as closely together relative the curves at higher  $q_m$ ). The simulation runs show that the signal buildup is sensitive to the type and variability of the size distribution. The skewness of the log-normal distribution appears to reduce the intensity of the signal in the long wavelength region, and cause the signal buildup curves to behave more like the actual sample. This effect is likely caused by the greater number of large diameter bubbles in the log-normal distribution, and is a likely reason for the similar slope ratios of the two experimental curves at lower  $q_m$ .

Figure (3-8) gives the simulated buildup functions for a log-normal distribution with four mean diameters and  $\sigma = 75$ . These curves display the sensitivity of the model for varying diameter length scales. The simulations show increased sensitivity to the bubble size as  $q_m$  increases. Note the change in relative spacing of the curves as the length scale of the simulation approaches the length scale of the emulsion. The form of the curves better approximates the form of the experimental data as the average diameter decreases. Figure (3-8) also shows the ratios of slopes for the linear fitted curves and respective mean diameters.  $m_1$  gives the slope for  $q_m = 6.42 \text{ mm}^{-1}$ ,  $m_2$  for  $q_m = 12.8 \text{ mm}^{-1}$ , and  $m_3$  for  $q_m = 19.3 \text{ mm}^{-1}$ . The slope ratios for the experimental data are  $\frac{m_1}{m_2} = 1.0426$  and  $\frac{m_2}{m_3} = 1.1914$ . The model slope ratios more closely resemble those of the data for smaller mean diameters, with a better fit occurring between  $140 - 160 \mu\text{m}$ .

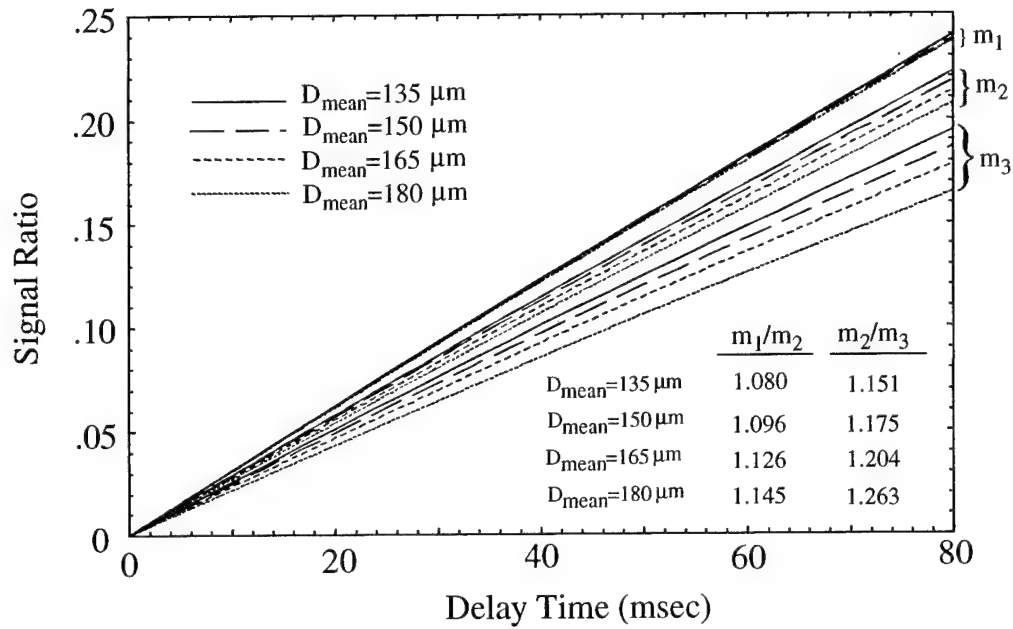


Figure 3-8: Comparison of buildup curves showing sensitivity to mean diameter

Next, consider the behavior of the signal as a function of  $q_m$ . The signal buildup reflects the behavior of the bubble's internal field. At low  $q_m$ , the water grating pitch is coarse, and many bubbles are located within one wavelength. The signal results from low-numbered harmonic functions of the dipolar field, and the fact that the field depends on the height of the bubble in the water grating. We expect little sensitivity to the bubble size for  $q_m$  in this range. This fact is confirmed by the experimental data, and the model. When  $\frac{2\pi}{q_m}$  is on the order of the bubble diameter, we expect the behavior to change from the more global effect discussed above, to a more local effect, where the internal field falls off as the center of the bubble is approached from the surface. In addition, as  $q_m$  increases, we expect the signal to decrease because fewer spins contribute to the signal at small wavelengths.

The experimental data in Figure (3-5) is grouped more closely together with respect to  $q_m$ , and we attribute part of this to the effect of the surrounding bubbles. At high  $q_m$ , the influence of a finite volume fraction is negligible, but at low  $q_m$ , the oil volume

fraction directly reduces the signal of the dipolar field. The low  $q_m$  buildup rate is thus somewhat lower than the model. At high  $q_m$ , water diffusion in the presence of the sample's susceptibility fields introduces an additional attenuation that also reduces the buildup rate.

The above results show that the DDF can be used to probe length scales in a system with bubble sizes that are too large to probe with other techniques, for example, Pulsed Gradient Spin Echo (PGSE) experiments. The presence of the inter-species mean field establishes a spatial cross-correlation across the interface, and the signal behavior contains information on the system's average structural characteristics. The extent of the spatial cross-correlation is limited by the range of the DDF, and diffusion in areas where susceptibility differences between phases create strong magnetic field gradients. Carr-Purcell Meiboom-Gill (CPMG) techniques may provide a means of overcoming these diffusive effects during the correlation time.

### **3.3 Conclusive Remarks Regarding Signal Physics**

This chapter has provided the solution to the "forward problem" regarding the DDF signal characteristics given a certain length scale distribution in a complex system. The study displays that the DDF signal inherently contains structural information, and a methodology has been developed to study DDF signal behavior in such systems. Future studies will build upon these results to solve the "inverse problem"; given a set of experimental results, what structural information can be obtained easily, and what scaling laws can be applied to confirm DDF behavior. The unique properties of the dipolar field enable its use in characterizing large scale systems, which can be used to complement PGSE studies.

## Chapter 4

# Signal Behavior and Interfacial Properties

The previous section described the derivation of the mean field generated by a modulated source magnetization, and the associated NMR signal generated within spherical bubbles of a different phase. Up to this point, the analysis has focused on solving the “forward problem”. That is, given a system with known characteristics, namely the bubble size distribution, the signal behavior can be forecast quite accurately. A more useful and powerful result is the solution of the “inverse problem”, in which NMR experimental results can be used to directly understand the characteristics of an unknown two-phase system. The solution of this problem requires that general scaling laws be developed to describe signal behavior versus experimentally controllable parameters, specifically, the wavelength of the applied magnetization grating. This chapter will focus on the development of these general results. The analysis provides much insight into the NMR behavior, and introduces new possibilities for the use of the technology, namely studying interfacial behavior.

Figure (4-1) provides a comparison of a numerical calculation of the signal intensity (blue line) to the experimental results (x's) versus the applied wavelength. The red dashed line will be discussed in the following section. The insets of this figure show the

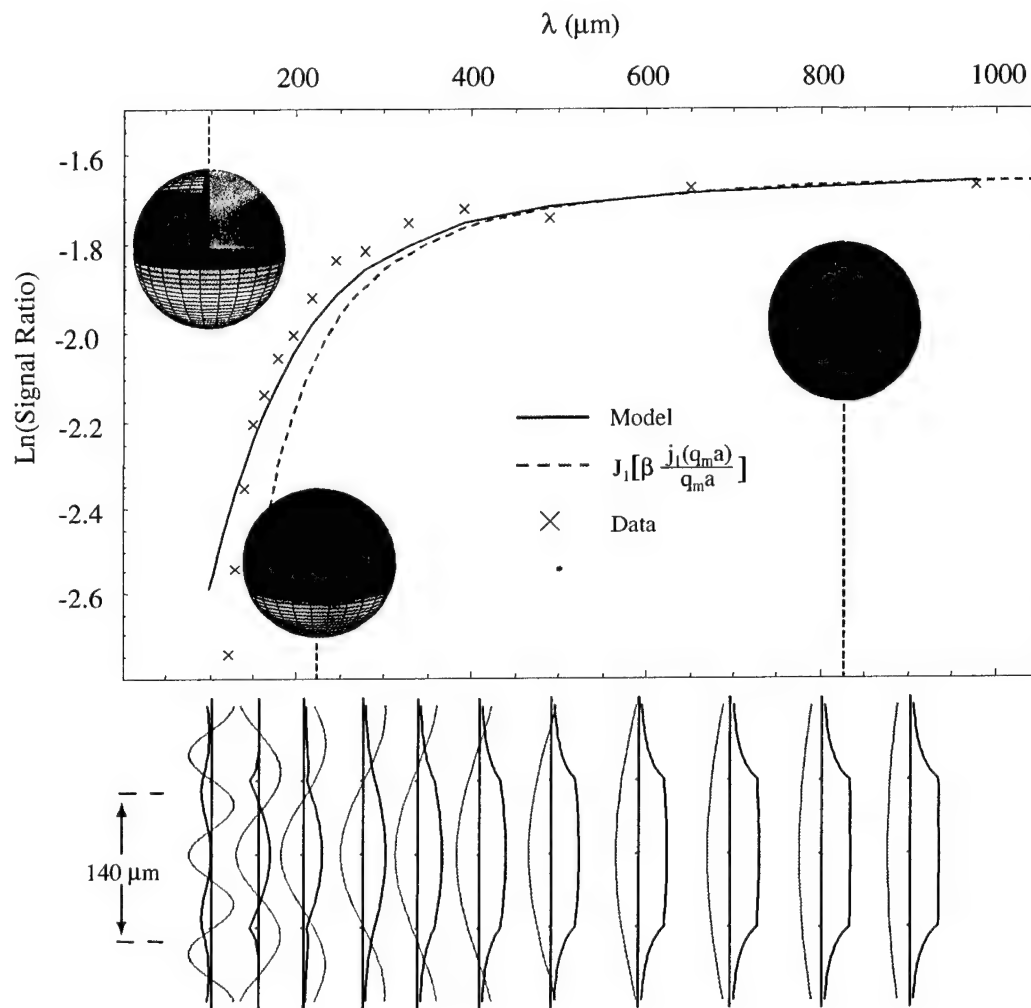


Figure 4-1: Variation of the signal ratio versus applied wavelength  $\lambda$ . Insets show field intensity.



calculated field intensity within the bubbles of radius  $a$ , at the indicated wavelengths. The north and south poles of the sphere lie on the  $z$ -axis. Red (+) and orange (-) show the highest intensities, and light blue indicates zero intensity. Note the change in behavior as the wavelength varies. At longer wavelengths the field is relatively uniform over the bubble. As the wavelength approaches the length scale of the system ( $140 \mu\text{m}$ ) the behavior changes and is localized near the interfacial regions of the bubble. In Figure (4-1), the series of plots below show the magnitude of the  $z$ -component of the magnetic flux density along the longitudinal axis of the bubbles. The water magnetization gratings (magnitude not to scale) are shown for comparison as the light gray curves that overlay the darker flux density curves. Note that the flux density along the center of the bubbles decreases in intensity as the wavelength decreases, giving rise to the interfacial dominant behavior. The NMR signal behavior will be described in detail and quantified by scaling laws in the following sections.

## 4.1 Scaling Behavior in the Long Wavelength Region

At long wavelengths, the variation of the field within a given bubble is small. The field in this region can be described by simplifying the lowest order harmonic that contributes to the mean field, the  $l = 1$  harmonic. After taking the limit of this term as  $R \rightarrow \infty$  and simplifying the result, the  $z$ -component of the field takes the following form,

$$H_z = \frac{2M_{o,water} \cos \phi}{a^3 q_m^3} [aq_m \cos(aq_m) - \sin(aq_m)] \quad (4.1)$$

where  $\phi = q_m \delta$ , in which  $\delta$  is the position offset as before. This equation can be simplified to give,

$$H_z = -2M_{o,water} \cos \phi \left[ \frac{j_1(aq_m)}{aq_m} \right] \quad (4.2)$$

where  $j_1$  is the first order spherical Bessel function of the first kind. Note that the only spatial variable in this equation is  $\phi$  which depends on the bubble's center position along the grating. Assuming no relaxation, the associated oil complex magnetization is,

$$M_{oil}^+ = M_{o,oil} e^{i\gamma\mu_o t 2M_{o,water} \cos\phi \left[ \frac{j_1(aq_m)}{aq_m} \right]} \quad (4.3)$$

Letting  $A = \gamma\mu_o t 2M_{o,water} \left[ \frac{j_1(aq_m)}{aq_m} \right]$ , the complex magnetization can be expanded to give,

$$M_{oil}^+ = M_{o,oil} e^{iA \sin(\phi + \frac{\pi}{2})} = M_{o,oil} \sum_{k=-\infty}^{\infty} e^{i(k\phi + \frac{\pi}{2})} J_k(A) \quad (4.4)$$

The  $\frac{\pi}{2}$  term in the exponential only contributes a phase, and will be neglected in this analysis. The normalized NMR signal is given by

$$\text{Signal Ratio} = \frac{1}{L} \int \sum_{k=-\infty}^{\infty} e^{ik\phi} J_k(A) e^{-iq_m z_{Lab}} dz_{Lab} \quad (4.5)$$

Assuming that the range of  $z \ll$  range of  $\delta$ , where  $\delta = \frac{\phi}{q_m}$ , and integrating over one cycle of the modulation so that  $L = \frac{2\pi}{q_m}$ , the following equation results,

$$\text{Signal Ratio} = \frac{1}{2\pi} \int \sum_{k=-\infty}^{\infty} e^{ik\phi} J_k(A) e^{-i\phi} d\phi \quad (4.6)$$

Only the  $k = 1$  term contributes to the signal in the experiment. When attenuation of the water is included, the resulting signal ratio is given by,

$$\text{Signal Ratio} = J_1 \left( \gamma\mu_o 2\kappa M_{o,water} \left[ \frac{j_1(aq_m)}{aq_m} \right] \right) \quad (4.7)$$

where  $\kappa$  is an attenuation variable that depends on water diffusion and the effect of the surrounding bubbles. For diffusive attenuation,  $\kappa$  is a time integrated variable and so incorporates the evolution time into Eqn. (4.7). In general  $\kappa$  is a complicated function of time. As  $q_m \rightarrow 0$ , Eqn. (4.7) approaches a constant that is independent of the

systems length scale. This function is displayed in Figure (4-1) as the red (dashed) curve, where  $\beta = \gamma\mu_o 2\kappa M_{o,water}$ . Note that this function is a good approximation to signal behavior until the wavelength approaches the length scale of the system. In the previous chapter, for modeling purposes,  $\kappa$  was determined by the product of the water volume fraction, relaxation of the transverse water magnetization while writing the grating, and unrestricted diffusive attenuation in the water grating. These factors provided a reasonable approximation to the attenuation of the signal. For Figure (4-1)  $\kappa$  was calculated by fitting the model curve to the two far right points of the experimental data to get  $\kappa = .49\tau_{evolve}$ , where  $\tau_{evolve}$  is the evolution time (80 msec). In general,  $\kappa$  is not linear in time, but for a given time, and neglecting water diffusion in the applied grating, this form is sufficient, and higher values of  $\kappa$  only serve to shift the model curve down in magnitude. Water diffusion in the applied gratings was not modeled for construction of Figure (4-1) in order to display the scaling behavior of the dipolar field. Simple estimates give reasonable values for  $\kappa$  as described below.

The presence of susceptibility fields in the water while writing the grating contributes to diffusion while the water magnetization is aligned in the  $z$ -direction. By estimating the bulk susceptibility field magnitude from the linewidth of the broadened portion of the water spectrum (144 Hz), this effect gives a diffusive time constant  $T_D \approx 88\text{msec}$ . Thus,  $\kappa$  will include the following factor

$$\kappa_{Susc,broad} \approx e^{-\tau_{crush}/T_D} \int_0^{\tau_{evolve}} e^{-t/T_D} dt = e^{-\tau_{crush}/T_D} T_D (1 - e^{-\tau_{evolve}/T_D}) = .54T_D = .59\tau_{evolve} \quad (4.8)$$

where  $\tau_{crush}$  is the time between the second water pulse and the oil pulse ( $\tau_{crush} = 9\text{ msec}$ ). The broadened water represents 63% of the total water in the spectrum. Accounting for this fact, and neglecting any attenuation in the narrow water gives

$$\kappa_{Susc} \approx \tau_{evolve} [.37 + .63 (.59)] = .74\tau_{evolve} \quad (4.9)$$

Combining the above susceptibility diffusion with the volume fraction (.76) and attenuation of the water on the transverse plane ( $e^{\frac{-5.6m\ sec}{T_{2,short}}} \approx .83$ ) results in a total attenuation estimate of  $\kappa \approx .47\tau_{evolve}$ . This figure is in reasonable agreement with the previous value of  $\kappa$  determined from fitting. A fully accurate solution to the signal attenuation requires additional research and more complex modeling incorporating the effects described above. Diffusive effects in the applied grating become very evident in the experimental data at wavelengths on the order of the bubble diameter, where the signal is localized to the interface. In addition, the volume fraction effect is expected to attenuate and flatten out the signal behavior as the wavelength increases, but its effect should lessen as the wavelength approaches the length scale of the system. This effect is displayed in the experimental data.

## 4.2 Scaling Behavior in the Short Wavelength Region

As the wavelength of the applied grating approaches the characteristic length scale of the system, the higher harmonics play a greater role in signal behavior. To analyze this behavior, a simplified model was used. The water was considered as a slab of magnetization that is of infinite extent in the  $x$  and  $z$  directions (see Figure 4-2); the  $z$ -direction is defined in the  $B_o$  direction). In the  $y$ -direction, the water slab extends from  $-\infty < y \leq 0$ . The water magnetization is described by

$$\vec{M}_{water} = M_{o,water} \cos(q_m z' + \phi) \hat{z} \quad (4.10)$$

$\phi$  is the phase of the magnetization at  $z' = 0$ , resulting from the height along the grating. The resulting field in the oil was calculated as a function of  $y$  and  $\phi$ . Again, the previously

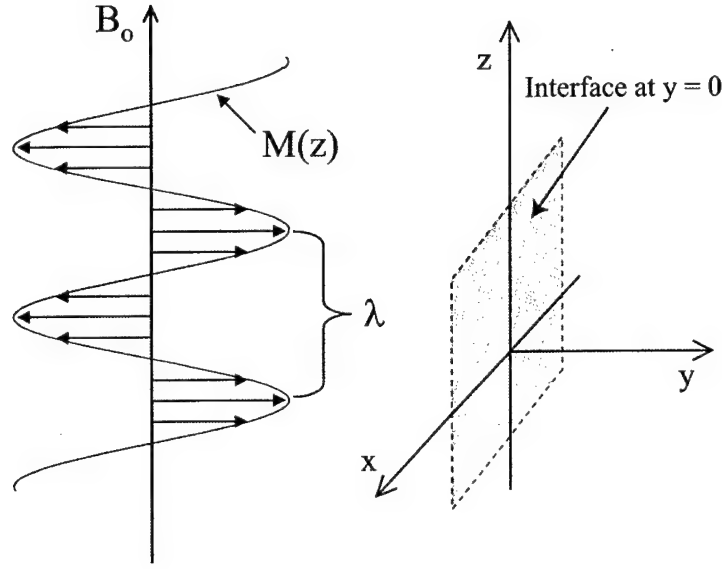


Figure 4-2: Coordinate system and problem setup for the slab problem.

described solution for Poisson's equation is used, repeated here for convenience,

$$\Phi = -\frac{1}{4\pi} \int \frac{\nabla' \cdot \vec{M}(\vec{r}')}{|\vec{r} - \vec{r}'|} d^3r' + \frac{1}{4\pi} \oint \frac{\hat{n}' \cdot \vec{M}(\vec{r}')}{|\vec{r} - \vec{r}'|} da' \quad (4.11)$$

The  $z$ -component of the field is found by taking the  $z$ -component of the gradient of Eqn. (4.11). The surface integral vanishes because the surface normal is perpendicular to the interface. After substitution of Eqn. (4.10), the following equation results,

$$H_z = \frac{M_{o,water} q_m}{4\pi} \int_{-\infty}^0 \int_{-\infty}^{\infty} \int_{-\infty}^{\infty} \frac{z' \sin(q_m z' + \phi)}{[x'^2 + (y - y')^2 + z'^2]^{3/2}} dz' dx' dy' \quad (4.12)$$

Integrating along  $z'$ , the result is

$$H_z = \frac{M_{o,water} q_m^2 \cos \phi}{2\pi} \int_{-\infty}^0 \int_{-\infty}^{\infty} K_o \left[ q_m \sqrt{x'^2 + (y - y')^2} \right] dx' dy' \quad (4.13)$$

where  $K_o$  is the zero-order modified Bessel function of the second kind. Now, let  $\hat{x}' = q_m x'$  and  $\hat{y}' = q_m y'$ , and then make the substitution  $\eta = y q_m$ . The result is

$$H_z = \frac{M_{o,water} \cos \phi}{2\pi} \int_{-\infty}^0 \int_{-\infty}^{\infty} K_o \left[ \sqrt{\hat{x}'^2 + (\eta - \hat{y}')^2} \right] d\hat{x}' d\hat{y}' \quad (4.14)$$

Eqn. (4.14) was integrated numerically. The solution was determined to be an exponentially decreasing function of  $\eta$  given by

$$H_z = \frac{M_{o,water}}{4} e^{-\eta} \cos \phi \quad (4.15)$$

Thus, the field directly depends on the height of the observation point along the grating, the distance from the interface, and the wavelength of the grating. Letting  $\phi = q_m z$ , the NMR signal ratio is given by

$$\text{Signal Ratio} = \frac{1}{2\pi a} \int_0^a \int_0^{2\pi} \text{Exp} \left[ -i\gamma\mu_o t \frac{M_{o,water}}{4} e^{-y q_m} \cos \phi \right] e^{i\phi} d\phi dy \quad (4.16)$$

where  $a$  is the distance over which  $y$  is integrated (for this model,  $a$  is the radius of the bubble). Using a Bessel function expansion similar to the previous section, integrating over  $\phi$ , neglecting unnecessary phase terms, and substituting  $\eta = y q_m$ , the following equation results

$$\text{Signal Ratio} = \frac{-i}{q_m a} \int_0^{\eta_{\max}} J_1 \left[ \gamma\mu_o t \frac{M_{o,water}}{4} e^{-\eta} \right] d\eta \quad (4.17)$$

Since  $0 \leq y \leq a$ , then  $\eta_{\max} = q_m a$ . For small arguments, the Bessel function can be given by its approximately linear form, resulting in

$$\text{Signal Ratio} = \frac{-i\gamma\mu_o t M_{o,water}}{8q_m a} \int_0^{\eta_{\max}} e^{-\eta} d\eta \quad (4.18)$$

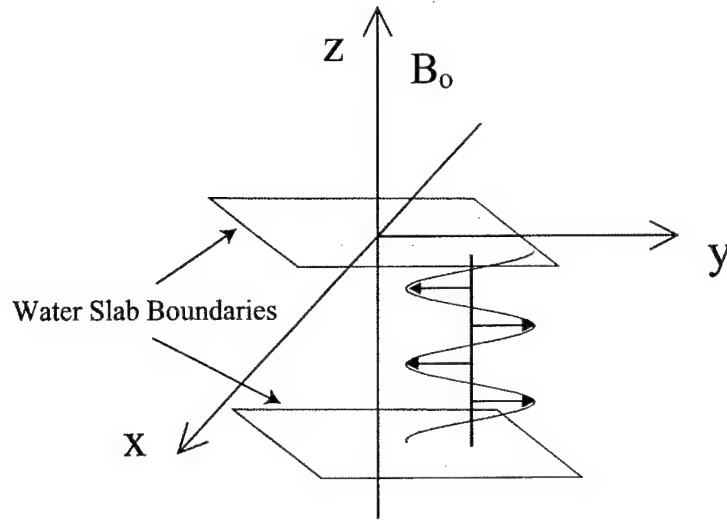


Figure 4-3: Coordinate system and problem setup for polar region calculation.

or

$$\text{Signal Ratio} = \frac{-i\gamma\mu_o t M_{o,water}}{8q_m a} (e^{-q_m a} - 1) \quad (4.19)$$

For  $q_m a$  in the range of interest, the exponential term can be safely neglected giving

$$\text{Signal Ratio} = \frac{i\gamma\mu_o t M_{o,water}}{8q_m a} \quad (4.20)$$

This result gives a  $q_m^{-1}$  dependence at short wavelengths that is displayed in Figure (4-1). To investigate this result, the field shape, as determined by the model of the previous section (using all harmonics up to eleventh order) was studied in regions close to the interface in transverse regions of a given bubble. The field shows approximately exponential behavior in these regions at high  $q_m$ .

In addition, another field calculation was performed to investigate field behavior in the polar regions of the bubble. For this calculation, another flat slab was assumed, but this time, it was oriented transverse to the applied water magnetization grating, see Figure (4-3). Eqn. (4.11) was again used, but now the surface contributions are

nonzero. The subsequent field integrations yielded constant field terms with respect to  $z$  for a given phase at the interface. The volume field terms cancels the surface terms yielding a zero field contribution from this geometry. Thus, there is zero contribution to the signal from this geometry, and the signal is dominated by the exponential behavior noted earlier, modified by the actual spherical shape of the real problem. Therefore, approximate  $q_m^{-1}$  behavior is used as the scaling law for NMR behavior in the region of short wavelengths.

### 4.3 Discussion

The scaling behavior described in the previous two sections provides a powerful novel means of using the dipolar field to extract the average length scale of a system. The first order harmonic dominates most of the signal behavior, and is responsible for a large bend in the curve at  $q_m a \approx 1$ . This result can be generalized to give  $\vec{q}_m \cdot \vec{\xi} \approx 1$ , where  $\vec{\xi}$  is a characteristic length along the measurement direction. For long wavelengths, the signal approaches a constant, and for short wavelengths, the signal falls off as  $q_m^{-1}$ . The rest of this section gives a brief discussion of the physics controlling the behavior and serves as a summary of the material described so far.

The method of using the mean dipolar field in NMR is an interesting and important example of breaking translational symmetry in order to impart a scale dependence. This phenomenon of magnetostatics is commonly investigated in physics<sup>1</sup>. The scattering (transfer of spatial spin gratings) via intermolecular macroscopic fields in NMR carries a signature of the local spatial distribution of the spin density. For arbitrary geometry, the inverse problem of extracting this spin distribution from experiments is intractable. However, there is a universal crossover in the scaling behavior at the sample's characteristic length scale  $\vec{\xi}$  of the species fluctuations in the sample along the measurement direction. This behavior has been demonstrated experimentally in the 100 micron-range

---

<sup>1</sup>Warren, W., Richter, W., Andreotti A., & Farmer B. "Generation of Impossible Cross Peaks Between Bulk Water and Biomolecules in Solution NMR" *Science*, **262**, 2005-2008 (1993).



for an oil-water emulsion, an important representation of complex, heterogeneous, soft matter.

In statistical physics the inverse problem of extracting microscopic correlation lengths and times from the observed macroscopic response is, in general, intractable. Simple scaling relations, such as the Ornstein-Zernike<sup>2</sup> relation, are of supreme importance, since they easily yield the underlying correlation lengths. Analogously, in the time domain, macroscopic relaxation rates often depend on the product  $\omega t$  of the microscopic correlation time  $t$  and the probe-frequency  $\omega$ . For example, the pioneering work of Blombergen, Purcell and Pound<sup>3</sup> extracted the microscopic correlation time  $t$  of water by noting the frequency  $\omega_c$  where the macroscopic relaxation rate changes rapidly as a function of the probing (Larmor) frequency.

The "scattering" or transfer of transverse spin magnetization in NMR experiments described here is carried by the magnetostatics dipolar mean field of one phase seen by the other. Remarkably, standard magnetostatics<sup>4</sup> is scale independent, and, as such, contains no information of the absolute size. When the translational symmetry is broken, by imparting on the system a spatially dependent magnetization, the well-known incipient logarithmic divergence due to dipolar fields is removed, and new interesting results emerge<sup>5</sup>. With a new scale available from that of the impressed symmetry-breaking field (SBF), it is possible to probe system length scales. The SBF becomes localized near the interface, and is quite analogous to a skin-depth phenomenon for a time-varying electromagnetic field in a dissipative medium (however, here we are concerned with the DC field). This localization near the interface provides a measure of the features near the interface.

A direct analogy to indirect-scattering can be expressed from the method in which a

---

<sup>2</sup>Ornstein, I. & Zernike, F. *Proc Acad Sci* (Amsterdam) **17**, 793 (1914)

<sup>3</sup>Blombergen, N., Purcell, E.M., & Pound, R.V. "Relaxation Effects in Nuclear Magnetic Resonance Absorption" *Phys. Rev.* **73**, 679-712 (1948).

<sup>4</sup>See for example, Maxwell, J. C. **Electricity and Magnetism**, 1st Ed, Clarendon Press, Oxford (1873) or Lord Rayleigh, *Phil. Mag.* **34**, 481 (1892).

<sup>5</sup>Deville, G., Bernier M., & Delrieux J. "NMR Multiple Echoes Observed in Solid He-3" *Phys. Rev. B* **19**, 5666-5688 (1979).

modulated SBF is exploited in the present case. A wave-vector dependence to the transverse magnetization is imparted first in one phase, which then is transferred to another phase and subsequently decoded. Recently, it has become well-appreciated<sup>6,7,8</sup> that an experiment where the wave vector dependent magnetization “grating” is encoded and subsequently decoded constitutes an “NMR-scattering” experiment with the scattering amplitude given by an intermediate scattering function completely analogous to that in neutron scattering. So far, most NMR scattering experiments deal with “self” scattering. The SBF experiments are unique in that they involve the transfer of the grating from one phase to another. These methods can extract the inter-phase Debye structure factors<sup>9</sup>, which are inter-phase spatial cross correlation functions.

In summary, this thesis has described a simple scaling law appropriate for NMR scattering involving dipolar fields. The characteristic length scale can be extracted from a crossover in scaling with the applied wavelength. In the long wavelength regime, the magnetization, and hence the NMR signal, approaches a constant. In the short wavelength regime, the signal is restricted to spins near the surface, and is proportional to  $\frac{\text{Surface Area} \times \lambda}{\text{Volume}} \propto \frac{1}{\vec{q} \cdot \vec{\xi}}$ . An observation of a crossover of shape in response near  $\vec{q} \cdot \vec{\xi} \approx 1$  can be used to extract the size  $\vec{\xi}$ .

## 4.4 Interfacial Velocity

Using the field determined for the parallel slab geometry given by Eqn. (4.15), this section will discuss the behavior of the field and NMR signal considering relative motion between the water slab and the oil region (see Figure 4-4). The experiment to be considered has a slab of water (in which the grating is written) sliding along a slab of oil (to which the magnetization is to be transferred). The relative motion is expected to impart a

<sup>6</sup>Cotts, R. M. *Nature* **351**, 443 (1991).

<sup>7</sup>Callaghan, P. T., Coy, A., MacGowan, D., Packer, K. J., & Zelaya, F. O. *Nature* **51**, 467, (1991).

<sup>8</sup>Cory, D. G. & Garroway, A. N. *Mag. Res. Med.* **14**, 435 (1990).

<sup>9</sup>Debye, P., Anderson, H. R., & Brumberger H. *J. Appl. Phys.* **28**, 679 (1957).

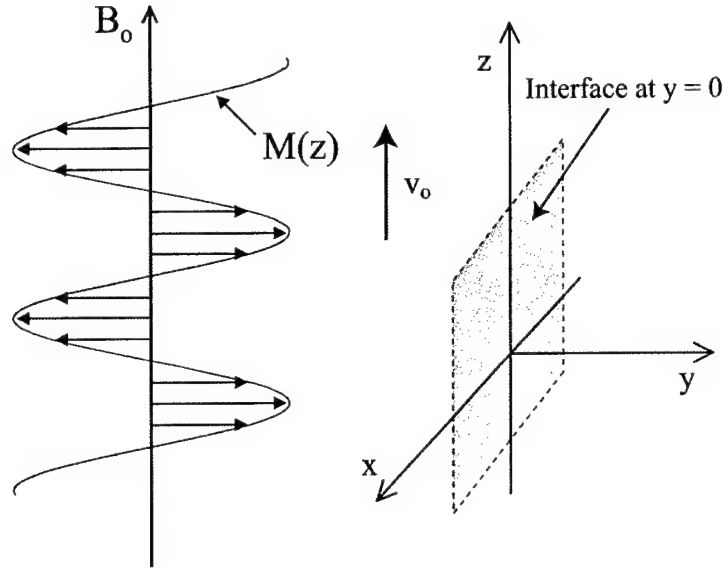


Figure 4-4: Coordinate system and problem setup for interfacial velocity calculation.

phase-to the NMR behavior of the oil spins. The phase difference can be measured for different evolution time intervals, and the velocity distribution can be inferred from a 2D Fourier transform of the resulting data set.

The initial analysis is simplified, and separates the transfer and buildup of the oil magnetization separate from the motion. First, the grating is written in the water. The resulting field generates Fourier components in the transverse oil magnetization, which are allowed to build up over a certain evolution time,  $\tau$ . The complex oil magnetization, neglecting relaxation, is represented by

$$M_{oil}^+ = -iM_{o,oil}J_1\left(\gamma\mu_o\frac{M_{o,water}}{4}\tau e^{-yq_m}\right)e^{iq_mz} \quad (4.21)$$

Following the buildup time, the water grating moves a distance,  $v_o t$ , where  $v_o$  is a constant water velocity, and  $t$  is the time of movement. Thus, the water magnetization phase changes by an amount,  $q_m v_o t$ , and the phase of the field, as seen by a spatially fixed oil test spin, changes accordingly. Following the final refocusing gradient, the relative

movement applies a phase term to the oil, and the resulting magnetization is

$$M_{oil}^+ = -iM_{o,oil}J_1 \left( \gamma\mu_o \frac{M_{o,water}}{4} \tau e^{-yq_m} \right) e^{iq_mv_ot} \quad (4.22)$$

Assuming that the argument of the Bessel function is small, the NMR signal ratio is just the previously derived signal from Eqn. (4.20), modified by the phase term giving

$$\text{Signal Ratio} = \frac{i\gamma\mu_o \tau M_{o,water}}{8q_ma} e^{iq_mv_ot} \quad (4.23)$$

In reality, the solution to this problem is not separated into a buildup time and a movement time. The evolution and movement terms must be integrated over a single time period. Neglecting relaxation, the complex magnetization is

$$M_{oil}^+ = M_{o,oil} \text{Exp} \left[ -i\gamma\mu_o \frac{M_{o,water}}{4} e^{-yq_m} \int_0^t \cos(q_m h_o + q_m v_o t') dt' \right] \quad (4.24)$$

where  $h_o$  is the initial longitudinal position of the grating before the velocity shift and signal buildup. The integral in the exponent can be evaluated as

$$\int_0^t \cos(q_m h_o + q_m v_o t') dt' = \frac{1}{q_m v_o} [\sin(q_m h_o + q_m v_o t) - \sin(q_m h_o)] \quad (4.25)$$

Simplifying and expanding into Bessel function form gives

$$M_{oil}^+ = iM_{o,oil}J_1 \left[ \frac{\gamma\mu_o M_{o,water}}{2q_m v_o} e^{-yq_m} \sin\left(\frac{q_m v_o t}{2}\right) \right] e^{iq_m h_o} e^{\frac{iq_m v_o t}{2}} \quad (4.26)$$

and the normalized signal ratio becomes

$$\text{Signal Ratio} = \frac{i}{a} e^{\frac{iq_m v_o t}{2}} \int_0^a J_1 \left[ \frac{\gamma\mu_o M_{o,water}}{2q_m v_o} e^{-yq_m} \sin\left(\frac{q_m v_o t}{2}\right) \right] dy \quad (4.27)$$

where  $a$  is the thickness of the oil slab.

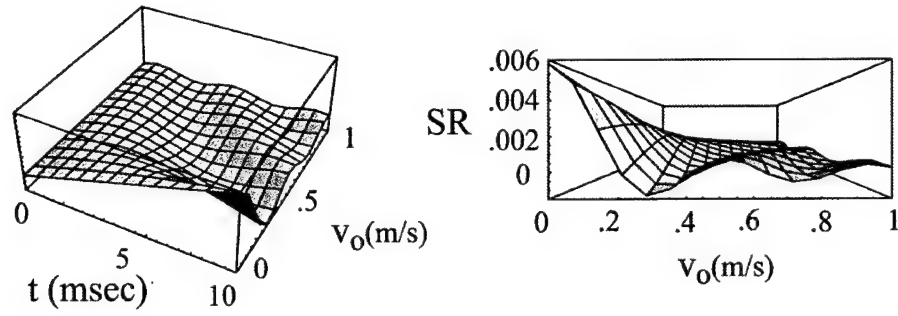


Figure 4-5: Plots of the signal ratio versus  $v_o$  and  $t$  for  $q_m = 3 \text{ mm}^{-1}$ .

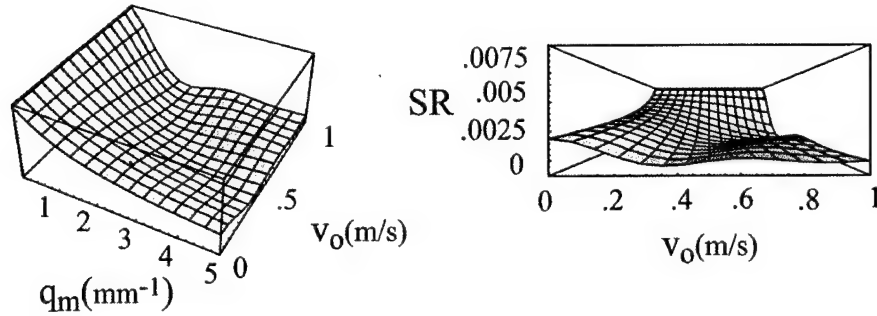


Figure 4-6: Plots of the signal ratio versus  $v_o$  and  $q_m$  for  $t = 5 \text{ msec}$ .

The solution to this simplified velocity problem shows that interfacial velocity measurements using the NMR dipolar field are possible, assuming that the signal phase change can be experimentally observed (i.e., the signal magnitude is high enough). The range of the field extending into the oil slab is given by  $e^{-yq_m}$ , and at high  $q_m$ , the velocity measurement is localized to the interface. The magnitude of the signal ratio for various parameters is shown in Figures (4-5, 4-6, and 4-7). Note that the signal is very small, and that there are regions where no signal is expected. This behavior is caused by translation of many periods of the water magnetization during the evolution time. For high relative velocities a different approach must be taken in order adequately build up a signal. Figure (4-8) displays one possible solution. Assuming that the grating is written in the water phase, the final  $\pi/2$  pulse on the oil is followed by its refocusing

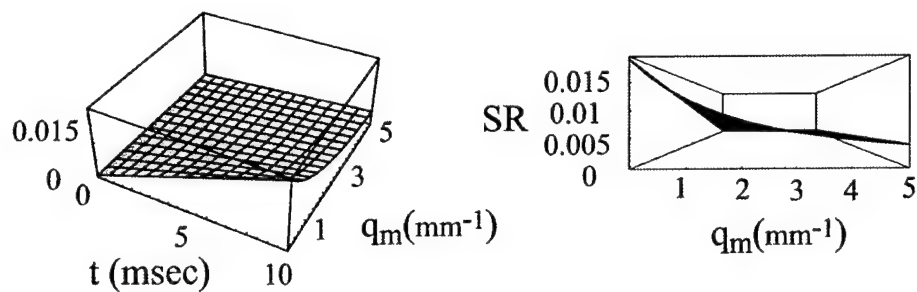


Figure 4-7: Plots of the signal ratio versus  $t$  and  $q_m$  for  $v_o = .01$  m/s.

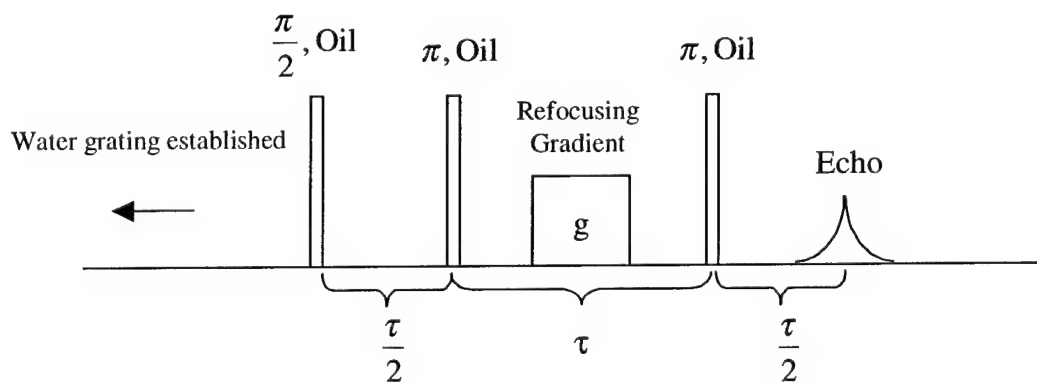


Figure 4-8: Example stroboscopic pulse sequence with  $n = 2$ .

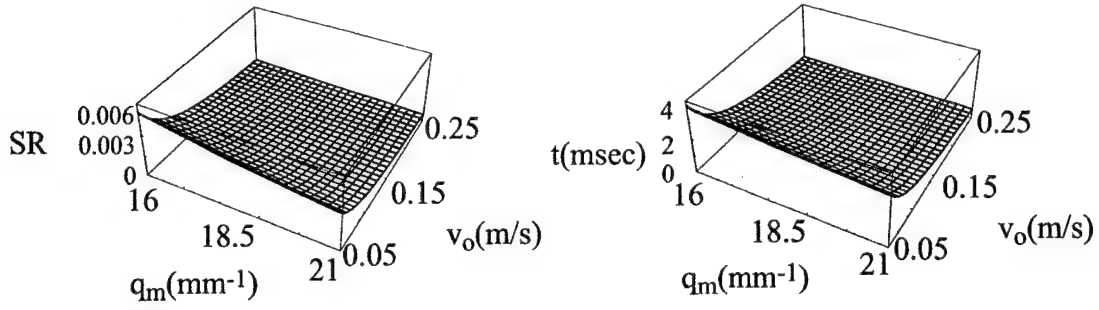


Figure 4-9: Plot of the signal ratio ( $n = 20$ ) and interval time for the stroboscopic velocity experiment.

gradient and several oil selective  $\pi$  pulses. The time interval,  $\tau$ , between each  $\pi$ -pulse is limited to the time for 1/2 cycle of the water magnetization to pass a given oil test spin, or  $\tau = \frac{\pi}{q_m v_o}$ . The  $\pi$  pulses selectively refocus the oil spins so that they evolve on the transverse plane in the presence of the water dipolar field. Although the water grating is not affected by the oil pulses, the sequence effectively shifts the phase of the water grating seen by the oil spins. Each evolution time interval is limited to 1/2 cycle of the water magnetization, and the overall effect is to build up the signal in the oil. The resulting signal ratio, neglecting attenuation, is

$$\text{Signal Ratio} = \frac{1}{a} \int_0^a J_1 \left[ \frac{n\gamma\mu_o M_{o,water}}{2q_m v_o} e^{-yq_m} \right] dy \quad (4.28)$$

where  $n$  is the number of  $\pi$  pulses after the oil  $\pi/2$  pulse. Thus the buildup time is determined by  $n$ ,  $q_m$  and  $v_o$ . Lower magnitudes of  $q_m$  and  $v_o$  will obviously give larger signal ratios. But the desired experiment is to map out the velocity distribution as the interface is approached (i.e., as  $q_m$  increases). Taking  $a$  to be 1 mm, the wavelength must be adjusted to limit the signal to regions that are smaller than  $a$ . Assuming  $q_m = 20 \text{ mm}^{-1}$ , the field extends out to  $\sim 250 \mu\text{m}$ , and should be a good estimate of a desired value for the experiment. Figure (4-9) shows a plot of the signal ratio for  $q_m$  in the above range for  $n = 20$ . Note that the magnitude of the signal is much higher

for this stroboscopic experiment for the desired  $q_m$  value. Figure (4-9) also displays intervals times of a few milliseconds. Velocity profiles can be obtained by limiting each buildup interval  $\tau$  to less than  $1/2$  cycle and then varying the time to achieve phase shifts. After  $n$  such intervals, the accumulated phase shift can be studied to infer the velocity. The above plots show that interfacial velocity measurements are feasible using oil and water phases. These phases have a relatively high equilibrium magnetization that leads to a high signal ratio. However, this analysis has not considered the effects of the velocity distribution at the interface. As the interface is approached from the side of the stationary phase, the velocity increases (caused by the shear stress at the interface). Further research must improve upon the constant velocity approximation to fully understand the effects of the actual velocity profile.

## 4.5 Interfacial Area

NMR is very conducive to accurately measuring the volume fraction of two particular species in a two-phase system. The areas under the respective NMR line shapes from a simple  $\pi/2$  pulse give the ratios of the number of spins in the system. For an example using proton spins, the volume fraction of each species can be calculated by knowing area ratios, together with the molecular weights, densities, and number of proton spins per molecule, from

$$\frac{\text{Area of Spin 1}}{\text{Area of Spin 2}} = \frac{\rho_1 V_1 (\# \text{ spins per molecule for species 1}) MW_2}{\rho_2 V_2 (\# \text{ spins per molecule for species 2}) MW_1} \quad (4.29)$$

and

$$\text{Total Volume} = V_1 + V_2 \quad (4.30)$$

The interfacial area can be estimated using knowledge of the average length scale obtained using the dipolar techniques. The dipolar technique gives some information about the



variability of the distribution of length scales in the system. This distribution can be modeled using a probability distribution as discussed in the previous chapter. Once the distribution has been estimated, the interfacial area calculation becomes very simple, and is demonstrated as follows. Tong and Tang<sup>10</sup> give the following equation for the interfacial area concentration in a two-phase system

$$a_i = n \int_0^{\infty} 4\pi a^2 f(a) da \quad (4.31)$$

where  $n$  is the bubble number density,  $a$  is the bubble radius, and  $f(a)$  is the probability density function of the radius. The term in the integrand is the average area per bubble. Analogously, the volume concentration can be written

$$v_i = n \int_0^{\infty} \frac{4\pi}{3} a^3 f(a) da \quad (4.32)$$

Therefore, the unknown  $n$  can be determined using the bubble volume fraction by

$$n = \frac{v_i}{\int_0^{\infty} \frac{4\pi}{3} a^3 f(a) da} \quad (4.33)$$

where  $v_i$  is the volume concentration of species  $i$ , as determined by the above process. Thus, the concentration of interfacial area becomes

$$a_i = \frac{3v_i \int_0^{\infty} a^2 f(a) da}{\int_0^{\infty} a^3 f(a) da} \quad (4.34)$$

---

<sup>10</sup>L.S. Tong and Y.S. Tang, **Boiling Heat Transfer and Two-Phase Flow**, Second edition, Taylor & Francis, 1997, p.163.

or

$$a_i = \frac{6v_i \int_0^{\infty} D^2 f(D) dD}{\int_0^{\infty} D^3 f(D) dD} \quad (4.35)$$

where  $D$  is the bubble diameter. For example, using the log-normal bubble diameter distribution of the previous chapter with  $D_{mean} = 150 \mu\text{m}$ ,  $\sigma = 75$ , and  $v_{oil} = 1 - .76 = .24$ , Eqn. (4.35) gives

$$a_i = 6.14 \text{ mm}^{-1} \quad (4.36)$$

Of course this value is subject to some error. The error of this result is mainly caused by inaccuracies in the model of the sample size distribution. This distribution was derived by comparing model results to experimental results. To get an accurate estimate of the error, the model must be refined to account for all effects on the shape of the signal, and then errors determined by comparison to the experimental signal behavior. In addition, use of the dipolar field inherently incurs a limit in resolution caused by diffusion of spins during the evolution time. For a given desired length scale measurement, a certain polarization must be realized to achieve a reasonable signal ratio. Tighter gratings corresponding to smaller length scales must be accompanied by higher polarizations. Figure (4-10) plots the required equilibrium magnetization versus length scale needed to perform the static length scale measurement (with Signal Ratio =  $SR = .01$ ) using water at various water diffusion coefficients. For this plot, water was assumed to be the transferring species, and oil is the species to which the magnetization was transferred. Note that for water at  $600\text{MHz}$  ( $M_o = .045380 \text{ A/m}$ ), with a diffusion coefficient of  $3 \times 10^{-9} \frac{\text{m}^2}{\text{sec}}$  the spatial resolution is limited to about  $14 \mu\text{m}$ . This resolution limit sets an error that is inherent in length scale measurements.

Figure (4-11) gives a plot of the required water magnetization needed to make a length scale measurement with a  $SR = .01$  in the presence of relative motion between the oil

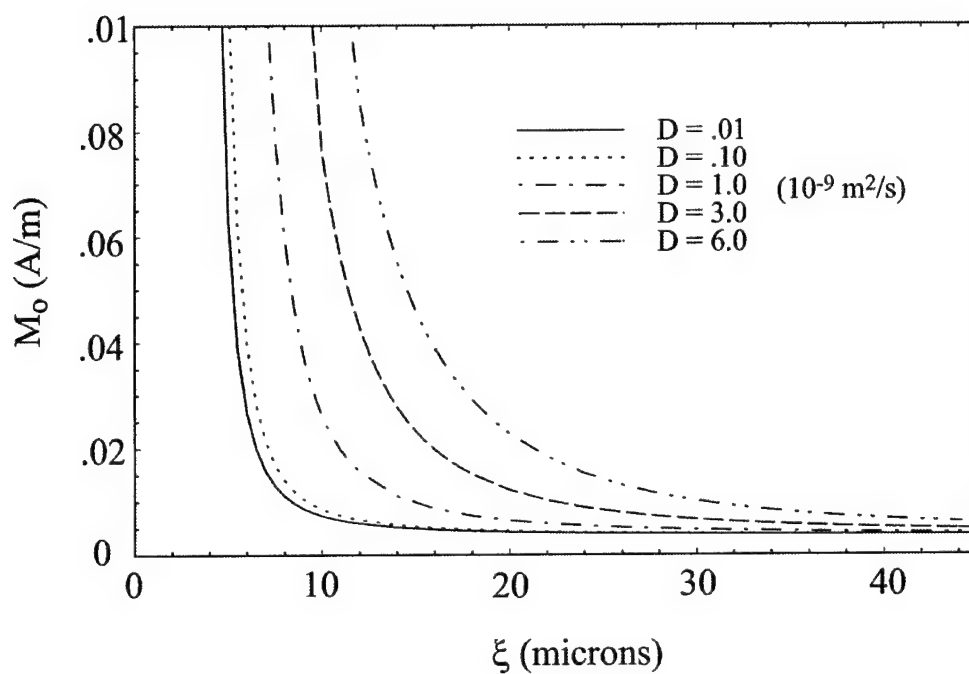


Figure 4-10: Required water equilibrium magnetization to achieve a  $SR = .01$  for static experiment.

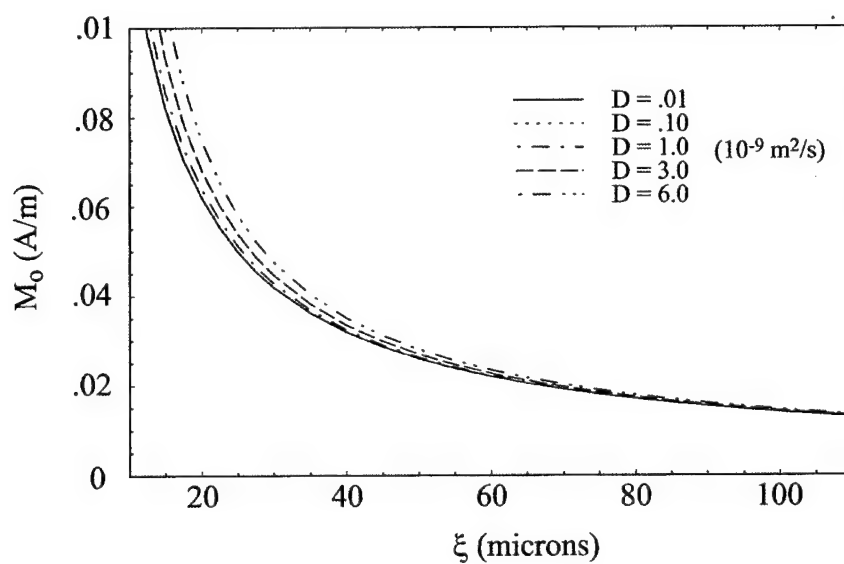


Figure 4-11: Required equilibrium water magnetization to achieve a  $SR = .01$  for  $v_o = .05$  m/s.

phase (bubbles) and the water phase. The relative motion has shifted the resolution to about  $30 \mu\text{m}$  for 600 MHz. The development of the model to make this plot deserves some explanation, and leads to some insights for future work in this area. The model uses the long wavelength scaling law, and takes into account relative motion and diffusion in the applied gradient plus some amount of attenuation caused by the volume fraction of water and susceptibility fields, assuming that the water was stationary and oil bubbles were translating through the medium at constant  $v_o = .05 \text{ m/s}$ . The stroboscopic experiment described earlier was used with 10  $\pi$ -pulses applied to the oil phase ( $n = 10$ ). For simplicity, the following discussion accounts for diffusion in the applied gradient only (susceptibility diffusion only adds a diffusive time constant to the problem, but complicates the math). The refocusing gradients in the oil phase have been divided into a series of gradient pulses between the  $\pi$ -pulses. Over the first time interval,  $\tau = \frac{\pi}{q_m v_o}$ , and neglecting diffusion in the oil phase, the oil magnetization is

$$M_2^+ = M_{o,oil} \text{Exp} \left[ i 2 \gamma \mu_o M_{o,water} \frac{j_1(q_m \xi)}{q_m \xi} \int_0^\tau e^{-D_{water} q_m^2 t} \cos(q_m h_o + q_m v_o t) dt \right] \quad (4.37)$$

After substituting  $\tau = \frac{\pi}{q_m v_o}$  the integral in the complex exponential becomes

$$\int_0^\tau e^{-D_{water} q_m^2 t} \cos(q_m h_o + q_m v_o t) dt = \frac{\left( e^{\frac{-D_{water} q_m \pi}{v_o}} + 1 \right) [D_{water} q_m \cos(q_m h_o) - v_o \sin(q_m h_o)]}{q_m (D_{water}^2 q_m^2 + v_o^2)} \quad (4.38)$$

Letting

$$A = 2 \gamma \mu_o M_{o,water} \frac{j_1(q_m \xi)}{q_m \xi} \frac{\left( e^{\frac{-D_{water} q_m \pi}{v_o}} + 1 \right) q_m D_{water}}{q_m (D_{water}^2 q_m^2 + v_o^2)} \quad (4.39)$$

and

$$B = 2\gamma\mu_o M_{o,water} \frac{j_1(q_m \xi)}{q_m \xi} \frac{\left(e^{\frac{-D_{water} q_m \pi}{v_o}} + 1\right) v_o}{q_m (D_{water}^2 q_m^2 + v_o^2)} \quad (4.40)$$

Eqn. (4.37) becomes

$$M_2^+ = M_{o,Oil} e^{i[A \cos(q_m h_o) - B \sin(q_m h_o)]} \quad (4.41)$$

This equation can be expanded by letting

$$\tan \phi = \frac{B}{A} = \frac{v_o}{q_m D_{water}} \quad (4.42)$$

to give

$$M_2^+ = M_{o,Oil} \sum_{l=-\infty}^{\infty} i^l J_l \left( \sqrt{A^2 + B^2} \right) e^{il\phi} e^{il(q_m h_o)} \quad (4.43)$$

Setting  $l = 1$ , and integrating over  $q_m h_o$  gives a signal ratio magnitude of

$$SR = J_1 \left[ 2\gamma\mu_o M_{o,water} \frac{j_1(q_m \xi)}{q_m \xi} \frac{\left(e^{\frac{-D_{water} q_m \pi}{v_o}} + 1\right)}{q_m} \sqrt{\frac{1}{q_m^2 D_{water}^2 + v_o^2}} \right] e^{i\phi} \quad (4.44)$$

The signal ratio still contains the structural information, but the magnitude has been modified by the relative velocity and the diffusion of each species. A similar function to Eqn. (4.44), modified by oil diffusion, a constant water diffusive attenuation, and accounting for the number of  $\pi$ -pulses, was used to make Figure (4-11).

## 4.6 Laser Polarized Xenon

This section will investigate the use of laser polarized Xe-129 as the second phase for the length scale experiment. Thus, the Xe takes the place of the oil in the previous

Properties	Water	Xenon (enriched)
Density ( $\frac{kg}{m^3}$ )	996.91	5.391
Molecular/Atomic Weight	18.02	131.29
Gyromagnetic Ratio ( $\frac{10^7 rad}{T \cdot sec}$ )	26.75	7.41
$M_{eq}$ at 600 MHz ( $\frac{A}{M}$ )	.04538	.003864 ( $P = 4\%$ )
$D$ at room temp/1 atm. ( $\frac{m^2}{sec}$ )	$2.5 \times 10^{-9}$	$5.6 \times 10^{-6}$

Table 4.1: Comparison of Xe-129 and Water Proton Properties

experiments. The use of a gas introduces additional factors into the problem. The greatest challenges to using Xe are its high diffusion coefficient, and its low density, resulting in low equilibrium magnetization.

The properties of enriched Xenon at a polarization ( $P$ ) of 4% are compared to those of water protons in Table (4.1). The natural Xe-129 abundance is 26.4% but this value can be raised to 100% with enrichment. Just about all of the properties of Xe negatively impact the ease of using it for dipolar experiments. The gyromagnetic ratio is lower by a factor of four, and the density is almost three orders of magnitude lower. These facts contribute to a low  $M_{eq}$  at a polarization of 4%, and give a much lower SNR than proton experiments with water. However, possibly the most limiting aspect of Xenon is its much higher diffusion coefficient. The high diffusion coefficient contributes significant attenuation during the buildup time, even using the stroboscopic experiment. Figure (4-12) gives the required equilibrium magnetization of water (transferring phase) to give a signal ratio in Xenon (receiving phase) of .01 for  $n = 10$ . The analysis used for the plot assumes that water surrounds Xenon and the relative velocity is .01 m/s. This relative velocity value corresponds to a typical bubble terminal rise velocity in bubbly flow for bubble diameters in the 1 mm range. The resolution is well in to the millimeter range ( $\sim 600 \mu m$ ) for water protons at 600 MHz for  $P = 4\%$ , and the experiment seems feasible for large length scales. Typical bubble diameters for two-phase flow models of bubbly flow are in the millimeter range (1 – 6 mm) with terminal rise velocities  $\sim .30$  m/s. As the Xenon polarization is increased, a lower equilibrium water magnetization is needed to achieve a given Xenon SNR, and a lower signal ratio can be tolerated. Thus,

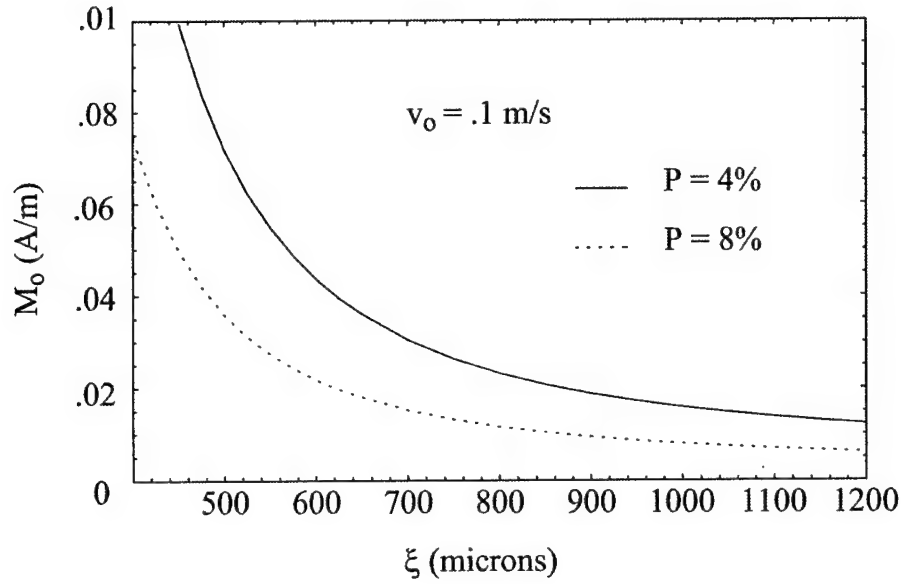


Figure 4-12: Required water equilibrium magnetization needed to achieve a Xe  $SR = .01$  ( $P = 4\%$ ) and  $SR = .005$  ( $P = 8\%$ ) for  $v_o = .1$  m/s.

the curve in Figure (4-12) shifts downward as  $P$  increases. If  $P$  is doubled to 8%, the resolution becomes  $\sim 500 \mu\text{m}$ . At the wavevector magnitudes in Figure (4-12), water diffusion is small and the curve shows very little variation with the diffusion coefficient of the surrounding medium. These results show that Xe experiments using the dipolar field will be very challenging, but are still worth pursuing in the future.

## Chapter 5

# Conclusion and Future Research

The goals of this thesis were stated in the introduction. The completion of each goal will now be discussed:

- 1) **Develop the underlying physical model used to extract structural information using the nuclear dipolar field from a relatively complex heterogeneous system.** The theory and model that were developed took a novel approach to solving the problem. The field was determined in real space, versus Fourier space. The physical field model provided valuable insight into the form of the field and the physics behind its behavior. The model that was developed to solve for the NMR signal of the emulsion sample provided a characteristic behavior that was used to determine the effects of different bubble radii and different size distributions. The model shows that the NMR signal is strongly influenced by the bubble size, and the variability in the size distribution can also be probed.
- 2) **Verify the physics and model by comparison to a static NMR experiment (emulsion system).** The emulsion sample provided an ideal tool for studying the effects of the dipolar field. The behavior of the model compared well with the behavior of the experimental results. By comparing the model to the experimental results, the size distribution was estimated, and the results compared well with



visual estimations of the actual bubble size distribution.

- 3) **Develop simple scaling laws that can be applied to easily extract length scale information.** Chapter 4 developed simple scaling rules that can be used to easily extract length scale information from experimental results. The signal behavior displays a characteristic change in scaling at  $\vec{q}_m \cdot \vec{\xi} \approx 1$ . At large wavelengths, the signal approaches a constant value. At short wavelengths, the signal falls off as  $q_m^{-1}$ . The change in behavior is attributed to the localized nature of the dipolar field. The majority of signal derives from distances located within  $1/2$  of the applied water magnetization wavelength, and as the wavelength approaches the length scale of the system, the field is necessarily restricted to the interfacial regions of the bubble. Thus the technique lends itself to future research on interfacial properties of these systems.
- 4) **Theoretically investigate use of the dipolar technique for studying interfacial velocity between two phases.** Also in Chapter 4, a theoretical investigation of interfacial behavior was launched. Two potential experiments were discussed. The first experiment consisted of a slab geometry where one phase was sliding over the other. The experiment simply allowed one phase to slide over the other over the evolution time. The pulse sequence was basically the same as the static experimental pulse sequence. The calculated signal ratios showed that interfacial velocity could be probed by measuring the phase shift associated with the sliding field. However, this experiment resulted in very small signal ratios, especially in the higher velocity regime, and the higher  $q_m$  values required to probe interfacial velocity. The second experiment consisted of a stroboscopic pulse sequence in which spin displacement over the time interval was limited to  $1/2$  wavelength of the sliding magnetization grating in the water. Selective  $\pi$ -pulses in the receiving phase, spaced at the correct time intervals, allow the signal to build up, and minimize the sliding effect on the signal strength while also allowing an

interfacial velocity measurement to be made. Future research could possibly map out the interfacial velocity profile for this slab geometry. However, the velocity profile effect on the NMR signal characteristics requires further research to fully understand.

- 5) **Investigate the feasibility of using the technique to make length scale measurements in two-phase flowing systems.** Finally, in Chapter 4, the feasibility of using the dipolar technique on flowing liquid-liquid and gas-liquid systems was examined. The strength of the signal is very strongly dependent on the polarization of the sample's net magnetization, and the diffusion of the spins of each phase. Diffusion in the receiving phase can be limited by using the stroboscopic pulse sequence described in Goal #4. For liquid-liquid systems, the feasibility of this technique is good, with length scale resolutions on the order of a few tens of microns for the relatively slow velocity used in the analysis. Higher relative velocities will be more challenging, yet the realization for future research seems very plausible. Future research is also necessary to fully explore the effect of disruption of the grating caused by movement of the bubbles through the water medium, and the effect that interfacial shear itself has on the signal characteristics. Further study of liquid-gas systems will be challenging. Gases have a very high diffusion coefficient, the effects of which can be lessened by using the stroboscopic sequence, and writing the magnetization grating in the water phase, while placing the gas in the receiving phase. In addition, gas (Xe) polarizations to date are low. Further improvements in the polarization technology may increase the success of studying these systems using the NMR dipolar technique.

## Appendix A

# Calculation of Equilibrium Magnetization

The equilibrium magnetization is calculated by determining the population difference between the two states for spin-1/2 nuclei.

$$\frac{N_{-o}}{N_{+o}} = e^{(-\frac{\gamma\hbar B_o}{kT})} \quad (\text{A.1})$$

For  $\nu_o = 600\text{MHz}$ ,  $B_o = 14.0926\text{T}$ ,

$$\frac{\gamma\hbar B_o}{kT} = \frac{(26.751 \times 10^7 \frac{\text{rad}}{\text{T} \cdot \text{sec}})(\frac{6.626}{2\pi} \times 10^{-34} \text{J} \cdot \text{sec})(14.0926\text{T})}{(1.381 \times 10^{-23} \frac{\text{J}}{\text{K}})(298\text{K})} = 9.59686 \times 10^{-5} \quad (\text{A.2})$$

Therefore,

$$\frac{N_{-o}}{N_{+o}} = e^{(-9.59686 \times 10^{-5})} = A \quad (\text{A.3})$$

$$M_{o,water} = \frac{\rho N_A (\# \text{ protons per molecule})}{M.W.} \left[ \frac{(1-A)}{(1+A)} \right] |\vec{\mu}_p| \text{ per proton} \quad (\text{A.4})$$

Using the high temperature approximation, this equation becomes,

$$M_{o,water} = \frac{\rho N_A (\# \text{ protons per molecule})}{M.W.} \frac{|\vec{\mu}_p|^2 B_o}{kT} \quad (\text{A.5})$$

Either of the above equations is sufficient. The proton magnetic moment is  $|\vec{\mu}_p| = \frac{\gamma \hbar}{2} = 1.41053 \times 10^{-26} A \cdot m$ . For water at room temperature ( $T = 25^\circ C = 298K$ ),  $\rho = 996.9096 \frac{kg}{m^3}$ ,  $M.W. = 18.0148 \frac{g}{mol}$ , and there are two protons per water molecule. Therefore,

$$M_{o,water} = .045380 \frac{A}{m} \quad (\text{A.6})$$

At  $\nu_o = 750 MHz$ ,  $B_o = 17.616T$  and

$$M_{o,water} = .056762 \frac{A}{m} \quad (\text{A.7})$$

Xenon-129 is laser polarized. The equation for the equilibrium magnetization of enriched Xe-129 is,

$$M_{o,Xe} = \frac{\rho N_A P |\vec{\mu}_{Xe-129}|}{A.W.}$$

where  $P$  is the polarization (assumed to be 4%). The Xe-129 magnetic moment is  $|\vec{\mu}_{Xe}| = \frac{\gamma \hbar}{2} = 3.90729 \times 10^{-27} A \cdot m$ . At room temperature and atmospheric pressure,  $\rho = 5.391 \frac{kg}{m^3}$ . Therefore,

$$M_{o,Xe} = .003865 \frac{A}{m} \quad (\text{A.8})$$

# Bibliography

- [1] Sangdoo Ahn, Natalia Lisitza, and Warren S. Warren, "Intermolecular Zero-Quantum Coherences of Multi-Component Spin Systems in Solution NMR", *Journal of Magnetic Resonance*, **133**, 1998, pp. 266-272.
- [2] A.S. Bedford, R. Bowtell, and R.M. Bowley, "Multiple Spin Echoes in Multicomponent Liquids", *Journal of Magnetic Resonance*, **93**, 1991, pp. 516-532.
- [3] J. Bibette, "Depletion Interactions and Fractionated Crystallization for Polydisperse Emulsion Purification", *Journal of Colloid and Interface Science*, Vol. **147**, No. 2, December 1991, pp. 474-478.
- [4] N. Blombergen, E.M. Purcell, and R.V. Pound, "Relaxation Effects in Nuclear Magnetic Resonance Absorption" *Phys. Rev.* **73**, 679-712 (1948).
- [5] R. Bowtell, R.M. Bowley, and P. Glover, "Multiple Spin Echoes in Liquids in a High Magnetic Field", *Journal of Magnetic Resonance*, **88**, 1990, pp. 643-651.
- [6] R. Bowtell, "Indirect Detection via the Dipolar Demagnetizing Field", *Journal of Magnetic Resonance*, **100**, 1992, pp. 1-17.
- [7] R. Bowtell and P. Robyr, "Structural Investigations with the Dipolar Demagnetizing Field in Solution NMR", *Physical Review Letters*, **76** (26), June 1996, pp.4971-4974.
- [8] P.T. Callaghan, **Principles of Nuclear Magnetic Resonance Microscopy**, Oxford University Press, Inc., New York, 1995.

- [9] P. T. Callaghan, A. Coy, D. MacGowan, K. J. Packer, and F. O. Zelaya, *Nature* **51**, 467, (1991).
- [10] J.G. Collier, **Convective Boiling and Condensation**, Third edition, Clarendon Press, 1994, pp. 34-41.
- [11] D.G. Cory and A.N. Garroway, *Mag. Reson., Med.*, **14**, 435.
- [12] R. M. Cotts, *Nature* **351**, 443 (1991).
- [13] P. Debye, H. R. Anderson, and H. Brumberger, *J. Appl. Phys.* **28**, 679 (1957).
- [14] G. Deville, M. Bernier, and J. Delrieux, "NMR Multiple Spin Echoes Observed in Solid  $^3\text{He}$ ", *Physical Review B*, Volume **19**, Number 11, 1 June 1979, pp. 5666-5687.
- [15] E. Fukushima, and S. Roeder, **Experimental Pulse NMR, A Nuts and Bolts Approach**, Addison- Wesley Publishing Company, 1981, pp. 218-219.
- [16] E.L. Hahn, "Spin Echoes", *Physical Review*, **80** (4), November 1950, pp. 580-594.
- [17] M. Ishii, Argonne National Laboratory, Private Communication, Letter to R. Nelson, Los Alamos National Laboratory, (July 1987).
- [18] J. D. Jackson, **Classical Electrodynamics**, Third Edition, John Wiley and Sons, Inc., 1999, p. 186.
- [19] S. Javelot, "Creation of an NMR device to Characterize Multi-phase Flows", Doctorate Thesis, Pierre and Marie Curie University, 1994.
- [20] J. Jeener, "Equivalence between the "Classical" and the "Warren" Approaches for the Effects of Long-Range Dipolar Couplings in Liquid Nuclear Magnetic Resonance", *J. Chem. Phys.*, **112** (11), March 2000, pp. 5091-5094.
- [21] R.F. Karlicek and I.J. Lowe, "A Modified Pulsed Gradient Technique for Measuring Diffusion in the Presence of Large Background Gradients", *Journal of Magnetic Resonance*, **37**, pp. 75-91 (1980).

- [22] Harold Körber, Elmar Dormann, and Goerg Eska, "Multiple Spin Echoes for Protons in Water", *Journal of Magnetic Resonance*, **93**, 1991, pp. 589-595.
- [23] S. Lee, W. Richter, S. Vathyam, and W.S. Warren, "Quantum Treatment of the Effects of Dipole-Dipole Interactions, in Liquid Nuclear Magnetic Resonance", *J. Chem. Phys.*, **105** (3), July 1996, pp. 874-900.
- [24] S. Levy, **Two-Phase Flow in Complex Systems**, John Wiley and Sons, Inc., 1999, pp.125-128.
- [25] I. Ornstein and F. Zernike, *Proc Acad Sci (Amsterdam)*, **17**, 793 (1914).
- [26] P. Robyr and R. Bowtell, "Nuclear Magnetic Resonance Microscopy in Liquids Using the Dipolar Field", *J. Chem. Phys.*, **106** (2), January 1997, pp. 467-476.
- [27] P. Robyr and R. Bowtell, "Measuring Patterson Functions of Inhomogeneous Liquids Using the Nuclear Dipolar Field", *J. Chem. Phys.*, **107** (3), July 1997, pp. 702-706.
- [28] C. P. Slichter, **Principles of Magnetic Resonance**, Third Edition, Springer, 1990, p. 66.
- [29] Olle Söderman, Balin Balinov, "NMR Self-Diffusion Studies of Emulsions", **Emulsions and Emulsion Stability** (edited by Johan Sjöblom), Surfactant Science Series Vol. **61**, 1996, pp. 369-392.
- [30] A. Sodickson and D.G. Cory, "A Generalized k-space Formalism for Treating the Spatial Aspects of a Variety of NMR Experiments", *Progress in Nuclear Magnetic Resonance Spectroscopy*, **33** (1998), pp. 77-108.
- [31] J. W. Spore et al., TRAC-M/FORTRAN 90 (VERSION 3.0) **Theory Manual**, U.S. NRC, July 2000.
- [32] Warren S. Warren, Wolfgang Richter, Amy Hamilton Andeotti, and Bennet T. Farmer II, "Generation of Impossible Cross-Peaks Between Bulk Water and Biomolecules in Solution NMR", *Science*, Vol. **262**, December 1993, pp. 2005-2009.

- [33] Warren S. Warren and Sangdoo Ahn, "The Boundary Between Liquidlike and Solidlike Behavior in Magnetic Resonance", *J. Chem. Phys.*, **108** (4), January 1998, pp. 1313-1325.
- [34] L.S. Tong and Y.S. Tang, **Boiling Heat Transfer and Two-Phase Flow**, Second edition, Taylor & Francis, 1997, p.163.